J. Fluid Mech. (2023), *vol*. 974, A38, doi:10.1017/jfm.2023.797

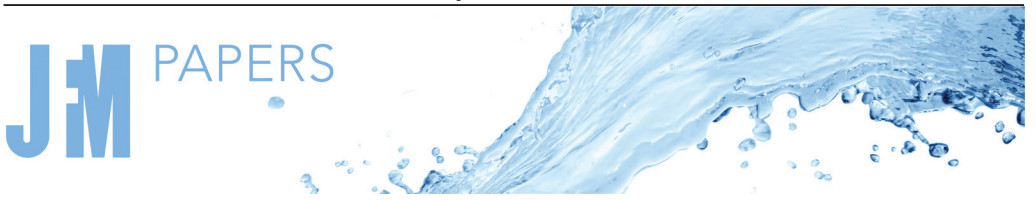

Conditional analysis on extreme wall shear stress and heat flux events in compressible turbulent boundary layers

Peng-Jun-Yi Zhang[1], Zhen-Hua Wan[1],†, Si-Wei Dong[2], Nan-Sheng Liu[1], De-Jun Sun[1],† and Xi-Yun Lu[1]

[1]Department of Modern Mechanics, University of Science and Technology of China, Hefei 230027, PR China

[2]State Key Laboratory of Aerodynamics, China Aerodynamics Research and Development Center, Mianyang 621000, PR China

(Received 10 March 2023; revised 12 July 2023; accepted 22 September 2023)

This study presents a comprehensive analysis on the extreme positive and negative events of wall shear stress and heat flux fluctuations in compressible turbulent boundary layers (TBLs) solved by direct numerical simulations. To examine the compressibility effects, we focus on the extreme events in two representative cases, i.e. a supersonic TBL of Mach number $M = 2$ and a hypersonic TBL of $M = 8$, by scrutinizing the coherent structures and their correlated dynamics based on conditional analysis. As characterized by the spatial distribution of wall shear stress and heat flux, the extreme events are indicated to be closely related to the structural organization of wall streaks, in addition to the occurrence of the alternating positive and negative structures (APNSs) in the hypersonic TBL. These two types of coherent structures are strikingly different, namely the nature of wall streaks and APNSs are shown to be related to the solenoidal and dilatational fluid motions, respectively. Quantitative analysis using a volumetric conditional average is performed to identify and extract the coherent structures that directly account for the extreme events. It is found that in the supersonic TBL, the essential ingredients of the conditional field are hairpin-like vortices, whose combinations can induce wall streaks, whereas in the hypersonic TBL, the essential ingredients become hairpin-like vortices as well as near-wall APNSs. To quantify the momentum and energy transport mechanisms underlying the extreme events, we proposed a novel decomposition method for extreme skin friction and heat flux, based on the integral identities of conditionally averaged governing equations. Taking advantage of this decomposition method, the dominant transport mechanisms of the hairpin-like vortices and APNSs are revealed. Specifically, the momentum and energy transports undertaken by the hairpin-like vortices are attributed to multiple comparable mechanisms, whereas those by the APNSs are convection dominated. In that, the dominant

† Email addresses for correspondence: wanzh@ustc.edu.cn, dsun@ustc.edu.cn

transport mechanisms in extreme events between the supersonic and hypersonic TBLs are indicated to be totally different.

Key words: compressible boundary layers, boundary layer structure

1. Introduction

Compressible turbulent boundary layers (TBLs) play an essential role in a wide range of practical flow configurations (Spina, Smits & Robinson 1994). From the fundamental perspectives, the TBL problems have been well established as a canonical type of wall turbulence to unravel the dynamical interaction of coherent structures associated with the wall quantities of practical importance, such as wall shear stress (WSS) and wall heat flux (WHF). To this end, a host of studies have been conducted over the past several decades to build up the physical links between the coherent structures and the WSS and WHF in TBLs. Although conceptual progress has been achieved, substantiation and quantification for such physical links remain open hot issues. To date, comprehensive studies dedicated to explore the generation mechanisms of skin friction and heat flux underlying the coherent structures are still highly desired, considering their potential applications in developments of advanced drag reduction technique and designs of efficient thermal protection (Marley & Riggins 2011; Zhang *et al.* 2020).

A significant feature of wall-bounded flows is that the intermittent, violent outward ejections of low-speed fluid and inrushes of high-speed fluid at a shallow angle towards the wall correspond to the majority of turbulent production. These frequent bursting motions result in the flatness of turbulent velocities near the wall being of a considerable magnitude (Farazmand & Sapsis 2017), indicating that significant deviations of flow quantities exist compared with their mean values. Consequently, large tails referring to extreme positive (EP) and negative (EN) fluctuations emerge in the probability density function (p.d.f.) (Guerrero, Lambert & Chin 2020), and these events that correspond to the large tails are the so-called extreme events. Blonigan, Farazmand & Sapsis (2019) studied extreme dissipation events in an incompressible turbulent channel flow and showed that large deviations or extreme events in turbulent wall-bounded flows are the consequence of persistent nonlinear energy transfers and extreme bursts associated with a transmission of energy from large scales of motion to the mean flow. Generally, extreme events are strongly coupled with coherent structures and flow dynamics.

1.1. *Coherent structures associated with extreme events*

The coherent structures associated with extreme events have attracted the keen research interest of the community. Sheng, Malkief & Katz (2009) performed concurrent measurement of WSS and the corresponding three-dimensional velocity field of a square duct channel at $Re_\tau = 1470$. Through conditional sampling based on the local maxima and minima of WSS, they identified two types of buffer layer structures that generate extreme stress events, namely the predominantly streamwise vortex corresponding to high WSS and the lifting spanwise vorticity corresponding to low WSS. Hutchins *et al.* (2011) conditionally averaged data obtained from measurement by hot-film sensors as well as hot-wire probes, and showed the presence of forward-leaning low- and high-speed structures above low and high skin-friction events, respectively. In addition, they regarded these skin-friction events as the footprints of large-scale superstructures. The rare backflow events within the viscous sublayer are related to EN events of WSS. Lenaers *et al.* (2012) investigated the rare backflow in channel flows by direct numerical

simulation (DNS), revealing that the rare backflow events are the consequence of a strong oblique vortex outside the viscous sublayer. By dividing the histogram of the large-scale WSS fluctuations measured from a TBL at $Re_\tau = 4000$ into four quartiles, Gomit, de Kat & Ganapathisubramani (2018) found the extreme events are associated with the large structures and in the modulation of the small scales by means of scale decomposition. Pan & Kwon (2018) numerically studied extremely high WSS events in a TBL and reported that they are induced by a finger-shaped large-scale sweeping region (Q4) extending from the outer layer to the wall. Cardesa *et al.* (2019) performed time-tracking of backflow regions in a turbulent channel flow and pointed out that backflow events seldom interact with each other. They demonstrated that backflow events result from a complex interaction between regions of high and low spanwise vorticity far beyond the viscous sublayer, and they are associated with the structures further away from the wall. Based on DNS data of a turbulent pipe flow at $Re_\tau = 1000$, Guerrero *et al.* (2020) revealed that an energetic quasi-streamwise vortex acts as an essential source of momentum at the near-wall region inducing EP events of WSS, whilst an identifiable oblique vortical structure along with two other large-scale roll modes is relevant to backflow events. To conceptualize the flow dynamics associated with extreme events, they proposed a three-dimensional model of the identified coherent structures.

As mentioned above, extensive investigations have been conducted on extreme events in the incompressible wall-bounded turbulent flow. However, as far as compressible flows are concerned, in which WHF becomes a crucial issue for thermal protections, much less work has been performed focusing on the extreme events of WHF. Recently, Tong *et al.* (2022) numerically studied the extreme events of both WSS and WHF in a compressible TBL at a free stream Mach number $M = 2.25$ and a Reynolds number $Re_\tau = 769$ with a cold-wall thermal condition. They revealed a pair of strong quasi-streamwise vortices, which transports high-speed fluid from the outer region towards the wall, inducing the sweep motion (Q4) that produces the EP events of WSS. In contrast, EP events of WHF are the result of the downward extrusion of low-temperature flow onto the high-temperature flow covering the wall. Recently, in high-Mach-number wall-bounded flows with sufficiently strong compressibility, the alternating positive and negative structures (APNSs) behaving as convecting wavepackets emerge near the wall (Yu, Xu & Pirozzoli 2019, 2020; Tang *et al.* 2020; Xu *et al.* 2021; Huang, Duan & Choudhari 2022; Zhang *et al.* 2022*b*). When APNSs are present, the wall pressure fluctuations will be greatly enhanced (Zhang *et al.* 2022*b*). Nonetheless, despite considerable progress in the study of extreme events, coherent structures associated with extreme events of WSS and WHF in a wall-bounded flow with much higher Mach number, such as the hypersonic TBLs in which APNSs emerge, had rarely been reported. Attributed to the close coupling of fundamental flow processes, e.g. shear, dilation and thermodynamics processes, in flow with high Mach number, WSS and WHF are closely related to each other, resulting in a significant difference from incompressible flow. Furthermore, the dynamics of the coherent structures associated with extreme events are not fully understood, deepening the quantitative analysis on how the structures transfer momentum and energy is directly beneficial to the physical insight.

1.2. *Integral identities on skin friction and heat flux*

Based on a wall-normal integration of the governing equations of flow, integral identities obtained allow us to quantify the contribution of the individual terms in a compact form, which represents the relevant transfer mechanisms of momentum or energy. Fukagata, Iwamoto & Kasagi (2002) derived an identity of the componential contributions that

different dynamical effects make to the frictional drag by a threefold repeated integration of the streamwise momentum equation, which is referred to as the FIK identity. The local skin friction is decomposed into laminar, turbulent, inhomogeneous and transient components. Peet & Sagaut (2009) extended the FIK identity to a fully three-dimensional situation allowing complex wall shapes. As a continuation of the work, Bannier, Garnier & Sagaut (2015) constructed a riblet flow model based on the extended FIK identity. Modesti *et al.* (2018) derived a generalized form of the FIK identity to quantify the effects of cross-stream convection on the mean streamwise velocity, wall friction and bulk friction coefficients in an arbitrarily shaped duct. Mehdi *et al.* (2014) proposed a modified form excluding explicit streamwise gradient terms, which can be applied for flows that change rapidly in the streamwise direction and flows with ill-defined outer boundary conditions. In addition, through these identities, flow control measures on skin friction can be quantified and further understood (Iwamoto *et al.* 2005; Kametani & Fukagata 2011; Kametani *et al.* 2015; Stroh *et al.* 2016). As for the regime of compressible flows, Gomez, Flutet & Sagaut (2009) generalized the FIK identity to a compressible turbulent channel flow to study compressible effects on skin friction. However, in their identity, only the components associated with viscosity variations were ascribed to compressible effects without thoroughly clarifying the compressibility effects on the various contributions (Li *et al.* 2019). Recently, Zhang & Xia (2020) derived FIK-like identities for the mean heat flux at the wall for the compressible turbulent channel flow, highlighting the importance of the viscous stress work in the near-wall region. Wenzel, Gibis & Kloker (2022) formulated twofold FIK-like identities based on compressible momentum and total-enthalpy equations to quantitatively assess the superordinate influences of compressibility, wall heat transfer and pressure gradient on momentum and heat transfer. Xu, Wang & Chen (2022) used similar twofold integral identities based on momentum and internal energy equations in hypersonic TBLs to explain the primary reasons for the overshoot phenomena of wall skin friction and heat flux. Generally, the FIK identities and their extended forms are valuable tools for studying the mechanisms of skin friction, heat flux and the corresponding control strategies.

Although the FIK property is widely used and has been developed considerably, one drawback is that some of the contributing terms are easily misinterpreted due to the straightforward threefold repeated integration on the momentum equation. The threefold repeated integration is mathematically sound but results in no physics-based explanation for the linearly weighted Reynolds shear stress by wall distance (Deck *et al.* 2014). Therefore, Renard & Deck (2016) derived an identity of mean skin friction from a mean streamwise kinetic-energy budget in an absolute reference frame which is named the RD identity. The RD identity interprets the turbulence contribution to the generation of skin friction in terms of the total production of turbulent kinetic energy. For a more physical interpretation of terms, Wenzel *et al.* (2022) proposed the FIK-like identities of skin friction and heat transfer by a twofold repeated integral on the momentum and total-enthalpy equations. They pointed out that the twofold repeated integral is fine, because the first integration gives a force/energy balance between the wall and all locations within the boundary layer; and the second integration represents its average in the wall-normal direction. In addition, the terms with a derivative in the wall-normal direction are presented without being linearly weighted by wall distance as in the classical FIK identity. Zhang, Song & Xia (2022*a*) compared four different identities of WHF derived by using the internal energy equation or the total energy equation through routines of the FIK and RD methods. They demonstrated that the twofold FIK-like identities based on the internal energy equation could straightforwardly provide a physical interpretation of WHF. However, all the above proposed identities are intended to describe the transport

mechanisms of momentum and energy in a mean state, which have to account for all events. In short, focusing on the transport mechanisms associated with extreme events, it is fundamentally desirable to develop identities of extreme WSS and WHF based on conditionally averaged governing equations.

1.3. *Methodology and goals of this study*

Based on the current progress of investigations on extreme events of WSS and WHF in wall-bounded flows, it can be concluded that the extreme events of WSS and associated coherent structures have been well investigated in the incompressible regime (Sheng *et al.* 2009; Gomit *et al.* 2018; Cardesa *et al.* 2019; Guerrero *et al.* 2020). However, the extreme events of WSS and WHF are much less studied in the compressible regime, and, in particular, relevant studies in hypersonic TBLs are still rare. Furthermore, despite the well-identification of the coherent structures associated with extreme events, the quantitative contributions of these coherent structures to WSS and WHF through different momentum and energy transfer mechanisms have not yet been explored. To this end, DNSs are performed to study extreme events of WSS and WHF in the compressible TBLs. Conditionally averaged fields are analysed to identify coherent structures associated with extreme events in both supersonic and hypersonic TBLs with the same temperature ratio between wall temperature T_w and recovery temperature $T_r = T_\infty(1 + r(\gamma - 1)M^2/2)$. Given the function of integral identities in characterizing the properties of momentum and energy transport mechanisms, we propose novel FIK-like twofold repeated integral identities of extreme WSS and WHF based on conditionally averaged streamwise momentum and internal energy equations, respectively, to quantitatively demonstrate how coherent structures associated with extreme events contribute to extreme events.

The rest of the paper is organized as follows: the DNS data set and corresponding simulation set-up are introduced in § 2. The fundamental statistic and instantaneous properties are illustrated in § 3 to provide an overall impression on WSS and WHF of the supersonic and hypersonic TBLs. Conditional analysis based on the volumetric conditional average and newly proposed integral identities is performed to identify coherent structures associated with extreme events and demonstrate the underlying momentum and energy transfer mechanisms in § 4. Finally, the new findings and conclusions are summarized in § 5.

2. Simulation set-up and database review

Guided by our previous work (Zhang *et al.* 2022*b*), DNSs have been performed for compressible cold-wall TBLs. The governing equations are the fully compressible Navier–Stokes equations as given in Appendix A. The coefficient of viscosity, μ, is a function of temperature and is calculated using Sutherland's law. The simulations are conducted based on the open-source code STREAmS (Bernardini *et al.* 2021), which can be accelerated by graphics processing units. A supersonic TBL with a free stream Mach number of $M = 2.0$ named M2T05 and a hypersonic TBL with free stream Mach number of $M = 8.0$ named M8T05 are simulated. The details of the database and numerical methods can be found in our previous work (Zhang *et al.* 2022*b*), and the simulation set-ups are reviewed briefly here. The equations are solved in a stretched Cartesian coordinate system by high-order finite-difference methods. A hybrid energy-preserving/shock-capturing scheme in a locally conservative form is used to perform the spatial discretization of the convective terms in the Navier–Stokes equations. In smooth (shock-free) regions of the flow, the convective flux is

Cases	$N_x \times N_y \times N_z$	$L_x \times L_y \times L_z$	Δx^+	Δy_w^+	Δy_e^+	Δz^+	N_f	$t_s u_\infty/\delta_i$
M2T05	2400×320×600	$55.7\delta_i \times 8.1\delta_i \times 8.7\delta_i$	9.9	0.76	10.6	6.0	204	589.4
M8T05	3600×320×400	$48.8\delta_i \times 6.8\delta_i \times 5.0\delta_i$	6.2	0.46	11.4	5.5	306	271.5

Table 1. The parameters of simulations: N_x, N_y and N_z are the numbers of grid points in three directions; L_x, L_y and L_z are the lengths of the physical computational domain based on the inlet boundary-layer thickness δ_i; Δx^+ and Δz^+ represent streamwise and spanwise grid spacings in the wall unit, respectively; Δy_w^+ and Δy_e^+ represent the wall-normal grid spacings at the wall and the boundary edge, respectively; N_f is the number of flow fields sampled for statistics and $t_s u_\infty/\delta_i$ is the period for ensemble averaging.

approximated by the eighth-order energy-preserving scheme (Pirozzoli 2010). Otherwise, in the discontinuous regions, the Lax–Friedrichs flux vector splitting ensures robust shock-capturing capabilities. The characteristic fluxes at interfaces are reconstructed by the seventh-order weighted essentially non-oscillatory scheme (Jiang & Shu 1996). The viscous terms are expanded to Laplacian form to avoid odd–even decoupling phenomena and are approximated with the sixth-order central finite-difference formulas. The three-stage, third-order Runge–Kutta scheme (Spalart, Moser & Rogers 1991) is used for time integration. To obtain a fully developed turbulent state, the inflow boundary condition is set by the recycling–rescaling procedure (Pirozzoli, Bernardini & Grasso 2010). At the upper and outflow boundaries of the computational domain, non-reflecting boundary conditions (Poinsot & Lele 1992) are imposed based on characteristic decomposition in the direction normal to the boundary. The bottom wall is set as a no-slip isothermal wall, using a similar characteristic wave treatment. A periodic boundary condition is applied in the spanwise direction. For thoroughly eliminating unphysical reflections, a sponge zone (Adams 1998) in combination with grid stretching is added at the top and tail of the computational domain.

Uniform grid spacing is used in the spanwise direction, and hyperbolic sine stretching is applied in the wall-normal direction. The grid spacing is uniform in the streamwise direction except at the end of the computational domain where stretching is applied. The parameters of simulation are shown in table 1. The grid resolutions used are comparable to other reliable DNSs of compressible TBLs (Zhang, Duan & Choudhari 2017; Bernardini *et al.* 2021; Huang *et al.* 2022; Xu *et al.* 2022). A higher resolution is achieved in M8T05 to capture finer turbulent structures. Various first- and second-order flow statistics have been validated by matching reference data in our previous work (Zhang *et al.* 2022*b*), verifying the sufficiency of grid resolutions. The number of flow fields and the period for statistics are enough for statistical convergence. The computational domain and vortical structures are plotted in figure 1. The vortical structures near the outlet are damped by the stretched grid and the buffer zone. The regions of fully developed flows are selected for analysis as $x/\delta_i \in [24.1, 48.4]$ for M2T05 and $x/\delta_i \in [27.8, 44.4]$ for M8T05, respectively, as highlighted in colours in figure 1. These regions are selected according to the distribution of the Reynolds analogy factor, which will be discussed in the following section. Parameters and statistical properties of the boundary layers at the centre locations of these domains are listed in table 2. The two boundary layers are compared based on very close friction Reynolds numbers Re_τ. The isothermal-wall temperature T_w of both TBLs are set based on the same ratio $T_w/T_r = 0.5$, where the recovery temperature is defined as $T_r = T_\infty(1 + r(\gamma - 1)M^2/2)$ based on a recovery factor of $r = 0.89$ (Zhang, Duan & Choudhari 2018). Meanwhile, the non-dimensional wall heat fluxes $-B_q$ are comparable in both cases.

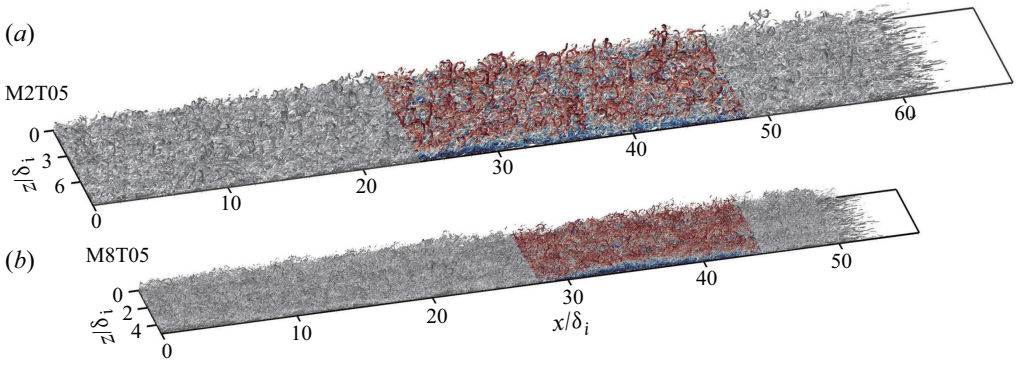

Figure 1. Computational domain and vortical structures illustrated by isosurface of Q-criterion. The domains selected for analysis are colourfully flooded by the streamwise velocity.

Cases	M	Re_δ	Re_τ	Re_{δ_2}	Re_θ	$\mathcal{H}$	$-B_q$	$T_\infty(K)$	T_w/T_r	Θ
M2T05	2.0	13 493	700	1507	1435	1.85	0.045	220.0	0.5	−0.202
M8T05	8.0	487 578	643	2772	15 701	17.00	0.052	51.8	0.5	0.456

Table 2. Parameters and statistical properties of the boundary layers at the centre location of the domain selected for analysis: $M = u_\infty/c_\infty$ and T_∞ are the free stream Mach number and temperature, respectively; $Re_\delta = \rho_\infty u_\infty \delta/\mu_\infty$ is the Reynolds number based on the boundary-layer thickness; $Re_\tau = \bar{\rho}_w u_\tau \delta/\bar{\mu}_w$ is the friction Reynolds number. The Reynolds numbers based on the momentum thickness are $Re_\theta = \rho_\infty u_\infty \theta/\mu_\infty$ and $Re_{\delta_2} = \rho_\infty u_\infty \theta/\bar{\mu}_w$. Additionally, $\mathcal{H} = \delta^*/\theta$ is the shape factor; $B_q = -(\mathrm{d}\bar{T}/\mathrm{d}y^+)_w/PrT_w$ indicates the non-dimensional wall heat flux; T_w/T_r means the ratio of isothermal-wall temperature to recovery temperature and $\Theta = (T_w - T_\infty)/(T_r - T_\infty)$ is the dimensionless temperature.

The database used has been well validated in our previous work (Zhang *et al.* 2022*b*), and we briefly review the results first. As shown in figure 2, compared with reference data, the distributions of u^+_{vd} reasonably agree with the wall law and the log law, where the superscript $(\bullet)^+$ denotes a quantity in the wall unit. However, the wall-cooling effects make the distributions shrink slightly in the viscous sublayer and overshoot in the log layer, in accordance with Zhang *et al.* (2018). The density-scaled turbulent intensity and Reynolds shear stress collapse well with the reference data (Pirozzoli & Bernardini 2011; Zhang *et al.* 2018), with larger magnitudes for M8T05 in the outer layer.

The simulation accuracy of the thermodynamic process is also confirmed by the faithful validation of velocity-temperature statistical properties shown in figure 3. The model of Zhang *et al.* (2014) is able to accurately predict the relation between mean temperature and velocity, while deviation is observed in the result of the equation of Walz (1969). Since the viscous heating and the development of the boundary layer are strongly coupled, the strong Reynolds analogy (SRA) allows the correlations that the velocity-temperature correlation coefficient $R_{uT} = -1$ and the turbulent Prandtl number $Pr_t = 1$, as long as the total temperature fluctuations are negligible (Morkovin 1962). As depicted in figure 3(*b*), in the highly cooled cases, it is obtained that $R_{uT} \approx 1$ near the wall, instead of the perfect anticorrelation between velocity and temperature fluctuations indicated by SRA. In the inner layer, R_{uT} is sensitive to the temperature ratio T_w/T_r; in the outer layer, R_{uT} shows a asymptotic behaviour of $-R_{uT} \approx 0.55$ (Huang *et al.* 2022). The turbulent Prandtl numbers Pr_t are consistent with the reference data (Zhang *et al.* 2018) in figure 3(*c*). A reasonable

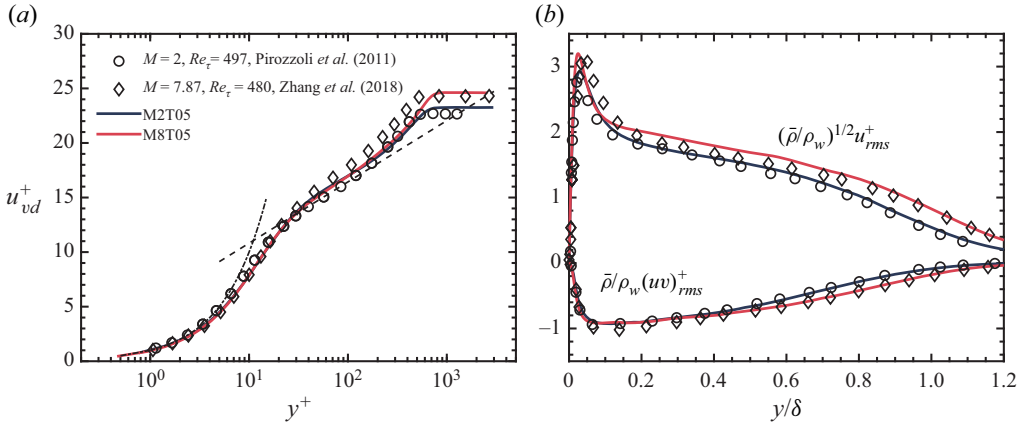

Figure 2. Statistical properties: (*a*) van Driest transformed mean velocity u^+_{vd}; (*b*) density-scaled turbulent intensity and Reynolds shear stress. —· – ·—, wall law $u^+_{vd} = y^+$; – – –, log law $u^+_{vd} = \log(y^+)/k + C$ with $k = 0.41$, $C = 5.2$.

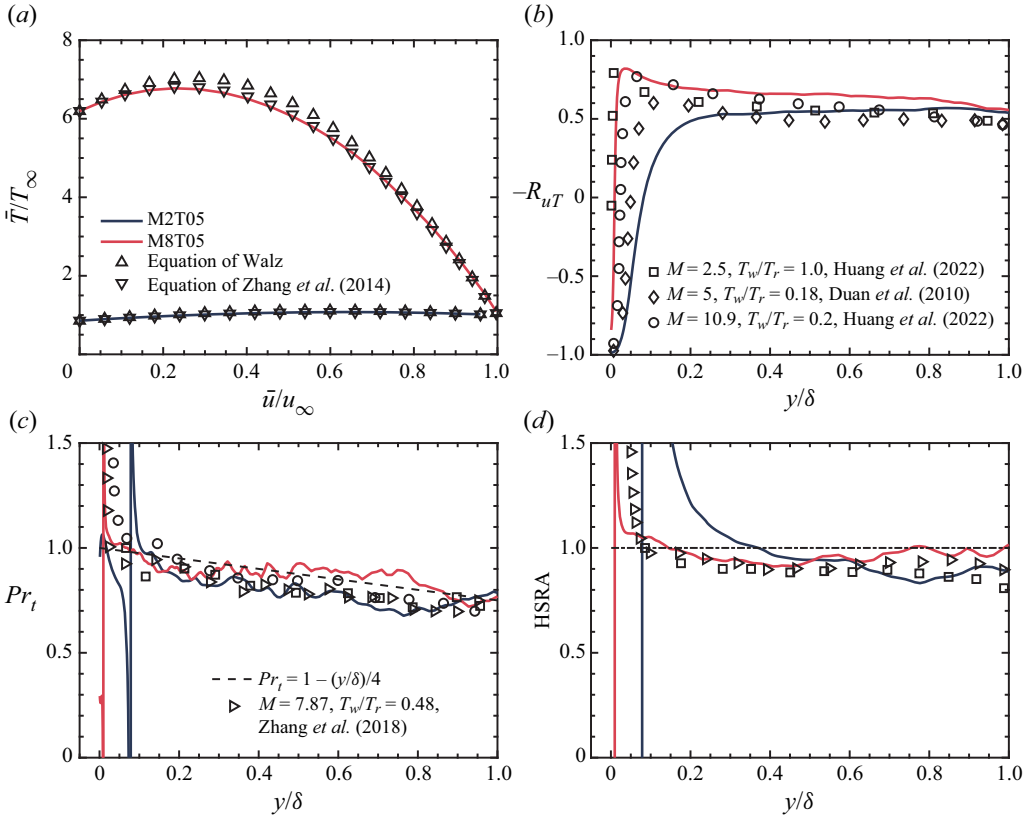

Figure 3. Velocity-temperature statistical properties: (*a*) the distribution of mean temperature $\bar{T}/T_\infty$ versus mean velocity $\bar{u}/u_\infty$; (*b*) the velocity-temperature correlation coefficient $-R_{uT}$; (*c*) the turbulent Prandtl number Pr_t; (*d*) the modified SRA of Huang, Coleman & Bradshaw (1995).

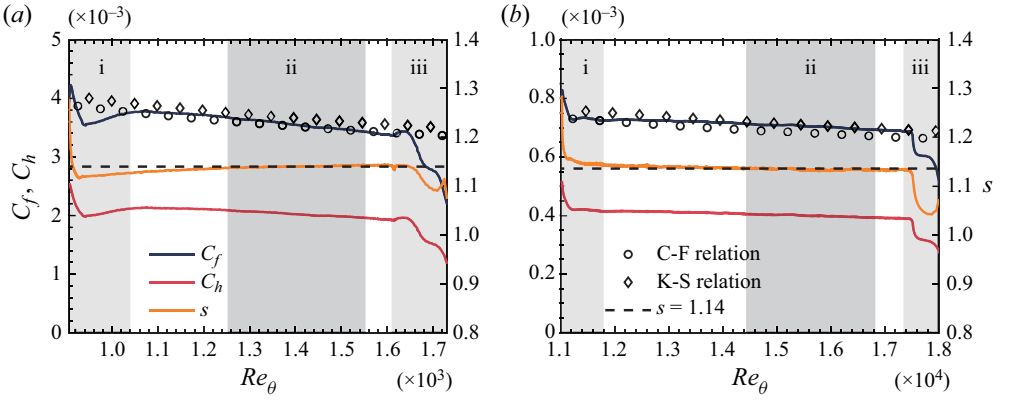

Figure 4. Skin-friction coefficient C_f, heat-transfer coefficient C_h and Reynolds analogy factor $s = 2C_h/C_f$ versus Reynolds number Re_θ for the cases (*a*) M2T05, (*b*) M8T05. The dashed line indicates $s = 1.14$, the symbols denote the incompressible relations of Kármán–Schoenherr (Roy & Blottner 2006) and Coles–Fernholz (Nagib, Chauhan & Monkewitz 2007) transformed by the van Driest II transformation. The lightly shaded regions (i) and (iii) mark the boundary layer developing region and the region influenced by buffer zone, respectively, and the shaded regions (ii) mark the domains selected for analysis.

prediction in the outer region of boundary layers can be provided by the linear relation $Pr_t = 1 - (y/\delta)/4$ proposed by Subbareddy & Candler (2011). Moreover, the modified SRA of Huang *et al.* (1995) (HSRA) is plotted in figure 3(*d*). The distributions of the present two cases are close to unity in the outer region of boundary layers and in agreement with the reference data (Duan, Beekman & Martín 2010; Huang *et al.* 2022).

3. Overall wall shear stress and heat flux

To depict a general picture of WSS and WHF in the supersonic and hypersonic TBLs, we begin by introducing the fundamental statistical and instantaneous properties in this section. Because of the strongly positive correlation of near-wall velocity and temperature fields shown in figure 3(*b*), the extreme events of WSS and WHF are probably related to the similar structures. For a more direct comparison, referring to Tong *et al.* (2022), the WSS and WHF are defined as

$$\tau_w(x, z, t) = \mu \frac{\partial u(x, y, z, t)}{\partial y}\bigg|_{y=0}, \quad q_w(x, z, t) = k \frac{\partial T(x, y, z, t)}{\partial y}\bigg|_{y=0}. \tag{3.1a,b}$$

The definition of q_w is analogous to that of τ_w with the same direction of the gradient, which is different to the conventional form. Figure 4 shows the distributions of the skin-friction coefficient $C_f = 2\bar{\tau}_w/(\rho_\infty u_\infty^2)$, heat-transfer coefficient $C_h = \bar{q}_w/(\rho_\infty u_\infty c_p(T_r - T_w))$ and Reynolds analogy factor $s = 2C_h/C_f$ as a function of the Reynolds number Re_θ. Two commonly used incompressible relations of $C_{f,i}$, namely the Kármán–Schoenherr relation (Roy & Blottner 2006) and modified Coles–Fernholz relation (Nagib *et al.* 2007), are transformed for comparison, written as

$$\left(C_{f,i}\right)_{KS} = \left(\log_{10}\left(2Re_{\theta i}\right)\left[17.075\log_{10}\left(2Re_{\theta i}\right) + 14.832\right]\right)^{-1}, \tag{3.2}$$

$$\left(C_{f,i}\right)_{CF} = 2\left(2.604\log Re_{\theta i} + 4.127\right)^{-2}. \tag{3.3}$$

According to the van Driest II transformation (Van Driest 1956), the skin friction of compressible TBLs can be estimated in terms of skin friction models for incompressible

TBLs through

$$C_f = C_{f,i}/F_c, \quad Re_\theta = Re_{\theta,i}/F_\theta. \tag{3.4a,b}$$

The transform coefficients F_c and F_θ are

$$F_c = \frac{T_r/T_\infty - 1}{\left(\sin^{-1} A + \sin^{-1} B\right)^2}, \quad F_\theta = \frac{\mu_\infty}{\mu_w}, \tag{3.5a,b}$$

where A and B are correlated to the boundary layer parameters; refer to Rumsey (2010) and Huang *et al.* (2022). Both the transformed relations reasonably describe the distributions of C_f in M2T05 and M8T05 with the cold wall. Specifically, the modified Coles–Fernholz relation performs better in M2T05 with $Re_\theta \sim O(1 \times 10^3)$, while the Kármán–Schoenherr relation has higher accuracy in M8T05 with $Re_\theta \sim O(1 \times 10^4)$. The Reynolds analogy factor is almost a constant $s \approx 1.14$ in the fully developed turbulent region for both cases. This constant is very close to the recommended value $s = 1.16$ by Chi & Spalding (1966) and Hopkins & Inouye (1971). In region (i), the turbulence is initialized by the recycling/rescaling inflow boundary condition, and in region (iii), the turbulence is damped by the buffer zone near the outlet. Thus, the domain for the following analysis is selected as region (ii), which guarantees a well-developed turbulent behaviour as it has far enough distance from region (i) and region (iii).

Figure 5(*a*) shows the p.d.f.s of normalized WSS and WHF fluctuations $\tau_w'/\tau_{w,rms}$ and $q_w'/q_{w,rms}$, where $\tau_{w,rms}$ and $q_{w,rms}$ are the root mean squares of WSS and WHF fluctuations, respectively. The distributions of p.d.f.s are consistent with a TBL of $M = 2.25$ and $T_w/T_r = 0.75$ (Tong *et al.* 2022), except for the negative tails. It is seen that the negative tails in M2T05 are suppressed by wall cooling, and strong viscous heating in M8T05 promotes the extreme heat transport to the wall. Generally, in both cases, the probabilities of the positive tails are significantly higher than those of the negative tails, and the profiles are highly positively skewed. As shown in table 3, the skewnesses of τ_w' and q_w' for both cases are positive, with the value approximating 1.0 except for S_τ of M8T05. In addition, the flatness F_q of M8T05 is much larger than that of M2T05, indicating much stronger intermittency in the q_w' fluctuation field for M8T05; thus, more intense extreme events of q_w' in M8T05 are expected. If the EP and EN events are defined by the same constant threshold as in the previous work (Pan & Kwon 2018; Tong *et al.* 2022), it will result in the number of EP events being far more than the number of EN events. Moreover, there has been no consensus on defining the threshold for extreme events (Guerrero *et al.* 2020). For the purpose of relevant comparisons and ensuring that the fluctuations in extreme events are extremely positive or negative, we define the EP/EN events as the strong positive or negative fluctuations in the first 1 %, respectively, which are marked by the shades in figure 5(*a*). In other words, the thresholds are chosen by making EP/EN events occupy a fixed percentage of total events, i.e. $\varepsilon = 1$ % in the present analysis. The thresholds of EP/EN events (ϕ_{tp}', ϕ_{tn}') can be determined by setting that the integral equations of p.d.f.s are satisfied as

$$\int_{\phi_{tp}'}^{\phi_{max}'} \mathcal{F}\left(\phi'\right) \mathrm{d}\phi' = \varepsilon, \quad \int_{\phi_{min}'}^{\phi_{tn}'} \mathcal{F}\left(\phi'\right) \mathrm{d}\phi' = \varepsilon, \tag{3.6a,b}$$

where ϕ' can represent the WSS/WHF fluctuations (τ_w', q_w'), and $\mathcal{F}(\phi')$ is the p.d.f. of the fluctuations. The specific thresholds of EP and EN events obtained are shown in table 4.

Regarding the joint p.d.f.s depicted in figure 5(*b*,*c*), the most probable combination of (τ_w', q_w') emerges in the third quadrant for both cases because of the cold-wall condition.

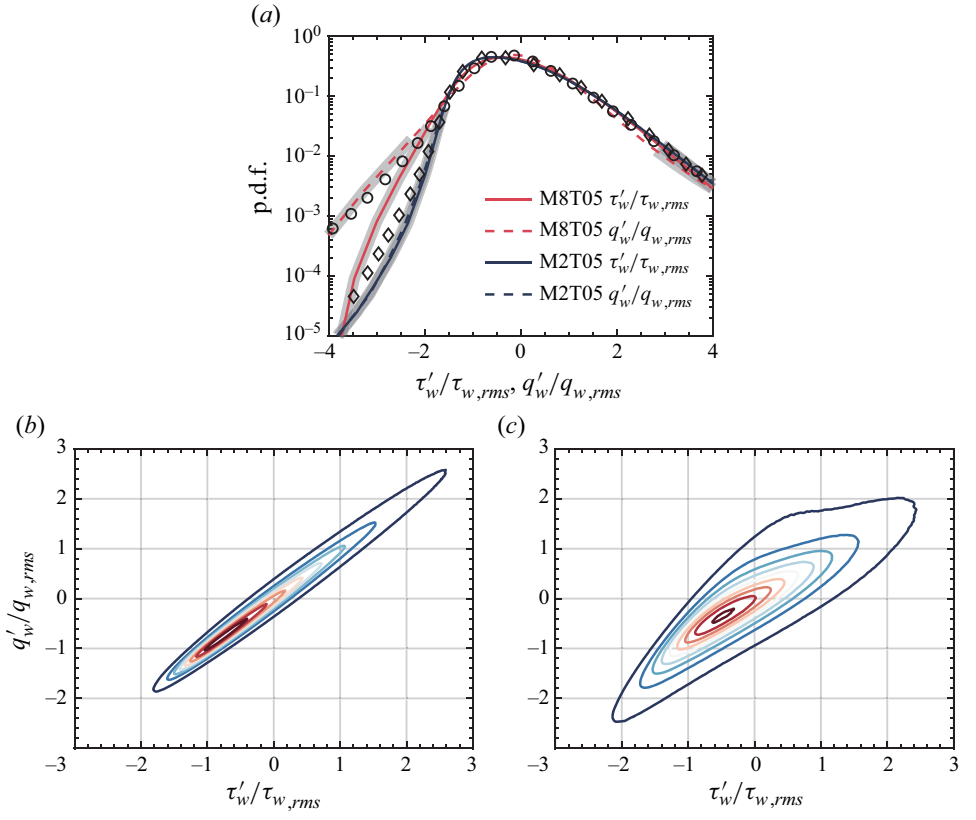

Figure 5. P.d.f.s of $\tau'_w/\tau_{w,rms}$ and $q'_w/q_{w,rms}$: (*a*) the distributions of single point p.d.f.s; the distributions of joint p.d.f.s for (*b*) M2T05 and (*c*) M8T05. The diamond and circle symbols indicate the p.d.f.s of τ'_w and q'_w in Tong *et al.* (2022) with $M = 2.25$ and $T_w/T_r = 0.75$, respectively. The shades mark the fluctuations belonging to extreme events. The values of joint p.d.f.s increase as the contour colours change from blue to red.

Case	$\tau^+_{w,rms}$	$q^+_{w,rms}$	S_τ	S_q	F_τ	F_q
M2T05	0.42	0.42	1.01	1.00	4.71	4.68
M8T05	0.45	0.75	0.82	1.07	4.85	11.74

Table 3. Statistics of WSS and WHF fluctuations: root-mean-square value $\phi_{rms} = \sqrt{\overline{\phi'^2}}$, skewness $S_\phi = \overline{\phi'^3}/(\overline{\phi'^2})^{3/2}$ and flatness $F_\phi = \overline{\phi'^4}/(\overline{\phi'^2})^2$.

Case	$\tau'_{w,tp}/\tau_{w,rms}$	$\tau'_{w,tn}/\tau_{w,rms}$	$q'_{w,tp}/q_{w,rms}$	$q'_{w,tn}/q_{w,rms}$
M2T05	3.02	−1.59	3.00	−1.61
M8T05	2.90	−1.91	2.87	−2.24

Table 4. Thresholds of extreme events for WSS and WHF fluctuations.

Obviously, the distribution of the joint p.d.f. for M2T05 shows a very elongated shape, i.e. τ'_w and q'_w tend to be highly positively correlated, which is consistent with the correlation coefficient in figure 3(*b*). For M8T05, the distribution of the joint p.d.f. shows an oyster-like shape, and the negative fluctuations of τ'_w and q'_w are more positively correlated

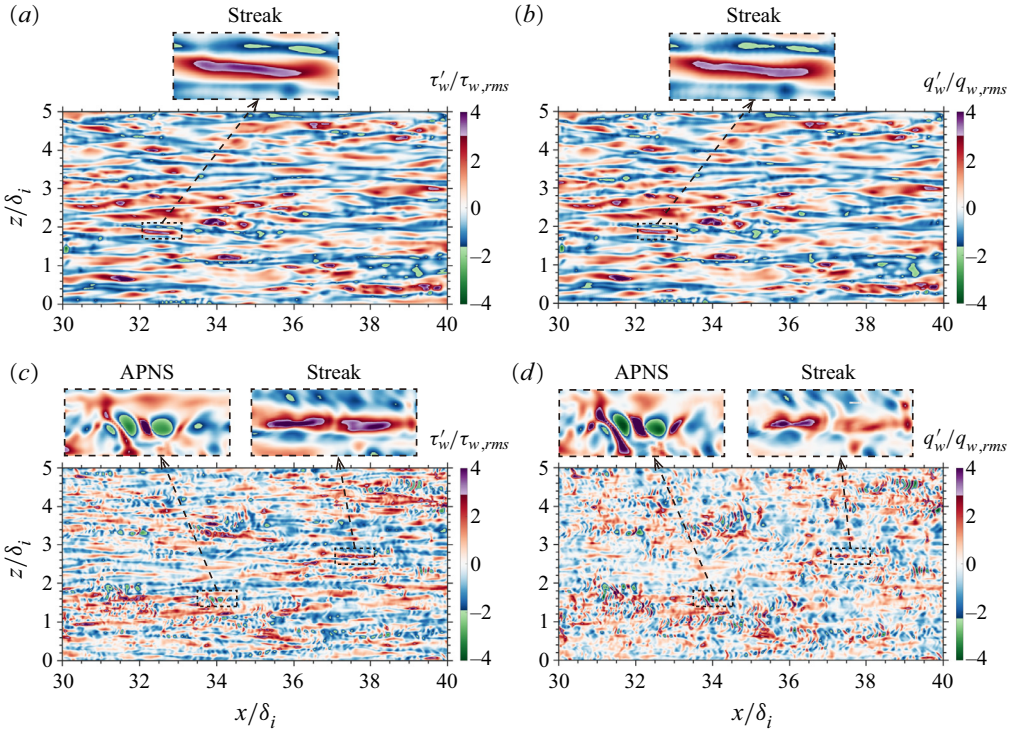

Figure 6. Instantaneous fluctuating fields of (*a*,*c*) $\tau'_w/\tau_{w,rms}$ and (*b*,*d*) $q'_w/q_{w,rms}$, for (*a*,*b*) M2T05 and (*c*,*d*) M8T05. The purple and green colour scales indicate EP and EN events, respectively. Two types of flow structures associated with extreme events, namely the streak and APNS, are enlarged in the upper panels for a clearer observation.

with each other than the positive counterpart. This is probably because heat conduction plays a key role in the combination of negative fluctuations ($\tau'_w < 0, q'_w < 0$). For the overall flow field of M8T05, wall streaks are the main structures. Due to wall-cooling effects, low-speed streaks are more probable to induce negative q'_w, while in high-speed streaks, other mechanisms such as viscous dissipation and convection become more important, which suppresses the correlation between τ'_w and q'_w.

To directly visualize the overall flow organization in the fields of τ'_w and q'_w, we plot the instantaneous fluctuating fields in figure 6. The additional purple and green colour scales are used to indicate EP and EN events, respectively. The τ'_w field of M2T05 shown in figure 6(*a*) is organized into elongated streamwise streaks of spanwise alternating positive and negative τ'_w, closely resembling the typical streaky patterns of velocity fields widely observed within incompressible and compressible TBLs (Jiménez *et al.* 2010; Pirozzoli & Bernardini 2011). The q'_w field shown in figure 6(*b*) is very similar to the τ'_w field, which is predictable based on the results of the joint p.d.f., implying the dominant role of heat conduction through the cold wall for M2T05. As enlarged in the upper panels, the flow structures associated with extreme events are mainly elongated streaks. Both EP and EN events of τ'_w and q'_w are favourable to emerge under high- and low-speed streaks, respectively. For M8T05, the fields of τ'_w and q'_w are more complicated. Apart from the typical flow structure of streaks, the travelling-wave-like APNSs are observed in both fluctuating fields. APNSs show a spotty form with a fine spatial scale, whose streamwise scale is far smaller than that of streaks. This kind of structure has been reported

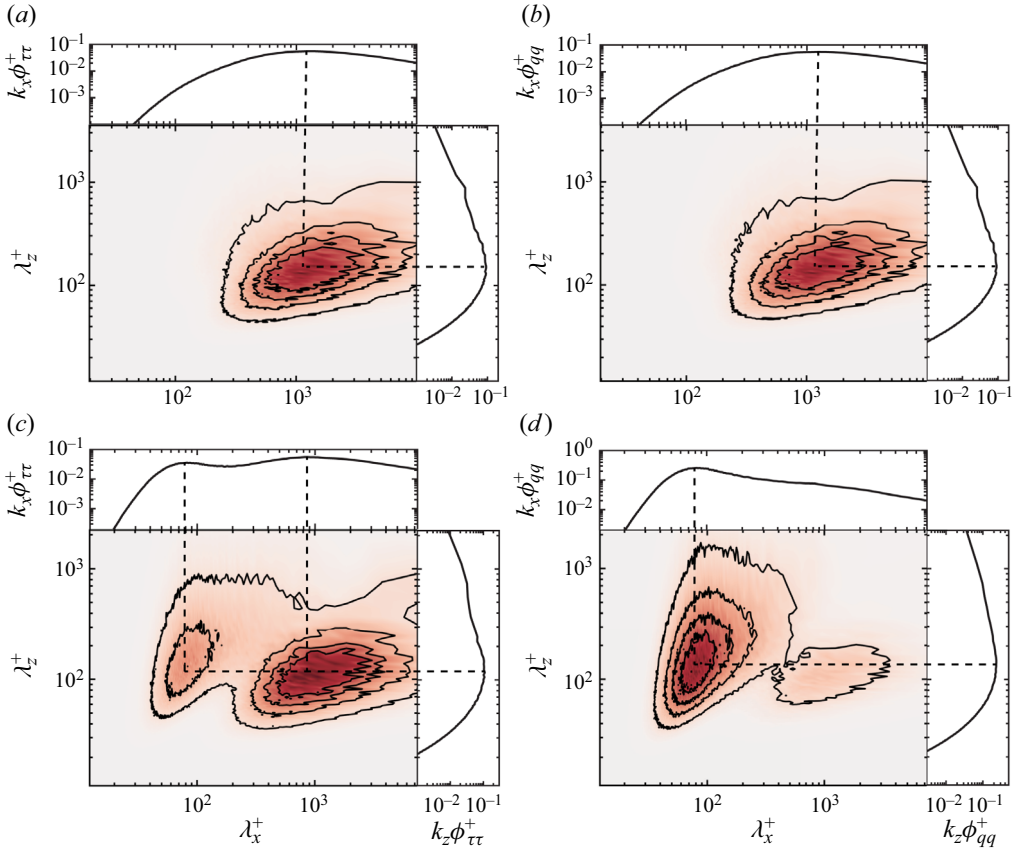

Figure 7. Two-dimensional pre-multiplied wavenumber spectra $k_x k_z \Phi^+(\lambda_x^+, \lambda_z^+)$ with integrated one-dimensional pre-multiplied wavenumber spectra $k_x\phi^+(\lambda_x^+)$ (top) and $k_z\phi^+(\lambda_z^+)$ (right) of (*a*,*c*) τ_w' and (*b*,*d*) q_w' for (*a*,*b*) M2T05 and (*c*,*d*) M8T05. The dashed lines correspond to the peak values in the one-dimensional spectra.

in high-speed wall-bounded turbulent flows in which compressibility plays a significant role, such as in channels (Yu *et al.* 2019; Tang *et al.* 2020) and boundary layers (Duan *et al.* 2010; Xu *et al.* 2021). APNSs were found to be closely related to dilatational motions and contribute to pressure fluctuations significantly (Zhang *et al.* 2022*b*). Generally, APNSs tend to concentrate within the cold low-speed streaks (Tang *et al.* 2020), in which the local sound speed is low enough, and the acoustic mode is strong enough to permit the cold streaks to act as the 'acoustic wave guides' (Coleman, Kim & Moser 1995). According to the results of stability analysis, APNSs tend to emerge in the cases of higher Mach numbers and lower wall temperatures (Hu & Zhong 1998; Tang *et al.* 2020). It is noteworthy that in the enlarged upper panels, these two kinds of flow structures, i.e. APNSs and streaks, are able to induce extreme events. An overall comparison shows that streaks seem to dominate in extreme events of τ_w', while APNSs seem to dominate in extreme events of q_w'.

Given the scale difference of streaks and APNSs, to show the spectral characteristics of τ_w' and q_w', two-dimensional pre-multiplied wavenumber spectra $k_x k_z \Phi^+(\lambda_x^+, \lambda_z^+)$ with integrated one-dimensional pre-multiplied wavenumber spectra $k_x\phi^+(\lambda_x^+)$ and $k_z\phi^+(\lambda_z^+)$ are plotted in figure 7. For M2T05, as shown in figure 7(*a*,*b*), the spectra of τ_w' and q_w' are quite similar to each other, yielding almost the same peak wavelengths of $\lambda_x^+ \approx 1200$ and

$\lambda_z^+ \approx 150$ indicated by the dash lines. These length scales agree with the typical near-wall streaks in the inner layer, reported in the incompressible TBLs (Hutchins & Marusic 2007) and compressible TBLs (Pirozzoli & Bernardini 2013). In addition, the wall-cooling effects increase the coherence of flow structures, and the spanwise peak wavelength becomes larger than the adiabatic case $\lambda_z^+ \approx 100$ which is also consistent with the trend found by Coleman *et al.* (1995). The characteristics of spectra become much more different for M8T05, as depicted in figure 7(*c*,*d*). Two local peaks are observed with nearly the same spanwise wavelength $\lambda_z^+ \approx 150$ as well as two distinct streamwise wavelengths $\lambda_x^+ \approx 80$ and $\lambda_x^+ \approx 900$. Accordingly, the peaks with finer and larger streamwise wavelengths are induced by APNSs and near-wall streaks, respectively. Due to the feature that APNSs prefer to concentrate within the low-speed streaks, the spanwise wavelengths of these two peaks are close. Consistent with the direct observation in figure 6(*c*,*d*), in the spectrum of τ_w', the dominant peak originates from streaks with $\lambda_x^+ \approx 900$, while in the spectrum of q_w', the dominant peak shifts to originate from APNSs with $\lambda_x^+ \approx 80$. This double-peak feature of wall quantity spectra has also been found in high-speed cooled channel flows (Yu *et al.* 2022) with bulk Mach number up to 4.79, implying that this is a general effect of the strong compressibility.

4. Conditional analysis on extreme events

In this section, to investigate the coherent structures associated with extreme events, we attempt to extract the coherent structures by means of volumetric conditional average at first. Then, to explore the physical mechanisms of how these coherent structures contribute to extreme τ_w' and q_w', we propose a novel decomposition method on conditionally averaged skin-friction and heat-flux coefficients. In this manner, the contribution of the momentum and energy transport mechanisms in extreme events can be quantitatively assessed.

4.1. *Conditionally averaged field based on extreme events*

For identifying the coherent structures associated with specific extreme events, the volumetric conditional average is commonly used (Pan & Kwon 2018; Cardesa *et al.* 2019; Guerrero *et al.* 2020; Tong *et al.* 2022). The conditionally averaged quantity is denoted as $\langle\bullet\rangle(\boldsymbol{x}, t)$. Referring to Pan & Kwon (2018) and Tong *et al.* (2022), the size of the average box is selected as $-300 < \Delta x^+ < 300$ and $0 < y^+ < 300$ in streamwise and wall-normal directions, respectively, as well as the whole spanwise domain for the sake of performing Helmholtz decomposition in the following. The indicative extreme τ_w' and q_w' are set at $\Delta x^+ = 0$, $\Delta z^+ = 0$ to locate the average box. The subscripts $\langle\bullet\rangle_{EP}$ and $\langle\bullet\rangle_{EN}$ represent the conditionally averaged quantities associated with EP and EN events, respectively.

Table 5 lists the parameters and results of the conditional average. The number of extreme events n_E exceeds 10^6, guaranteeing the convergence of the conditional average. The ratios of the conditionally averaged skin-friction coefficient to the overall skin-friction coefficient $\langle C_f\rangle_{EP}/C_f$ are approximately the same for both cases, while the ratios of the conditionally averaged heat-transfer coefficient to the overall heat-transfer coefficient $\langle C_h\rangle_{EP}/C_f$ for M8T05 is much larger than that for M2T05, also implying the more intense extreme events in the q_w' field for M8T05. Furthermore, associated with extremely negative events, $\langle C_f\rangle_{EN}$ and $\langle C_h\rangle_{EN}$ for M8T05 become negative values, implying flow states of backflow and reverse heat transfer in the sense of conditional average. According to the conditionally averaged coefficients, it can be expected that the transports of momentum and energy in extreme events are much more intense than those in mean flow. Due to the strong positive correlation of τ_w' and q_w' for M2T05, the fluctuations that coexist in extreme

https://doi.org/10.1017/jfm.2023.797 Published online by Cambridge University Press

Case	$n_E \times 10^{-6}$	C_f	$\langle C_f \rangle_{EP}$	$\langle C_f \rangle_{EN}$	C_h	$\langle C_h \rangle_{EP}$	$\langle C_h \rangle_{EN}$	P_{EP}	P_{EN}
M2T05	1.23	3.5×10^{-3}	9.1×10^{-3}	9.4×10^{-4}	2×10^{-3}	5.2×10^{-3}	5.0×10^{-4}	86 %	76 %
M8T05	1.45	7.0×10^{-4}	1.9×10^{-3}	-1.3×10^{-5}	4×10^{-4}	1.6×10^{-3}	-4.1×10^{-4}	43 %	69 %

Table 5. Parameters and results of conditional average: n_E is the sample number of extreme events; C_f and C_h are the skin-friction and heat-transfer coefficients, respectively; $\langle C_f \rangle$ and $\langle C_h \rangle$ indicate the conditionally averaged skin-friction and heat-transfer coefficients, respectively; P is the percentage of the events which coexist both in extreme τ_w' and q_w' events.

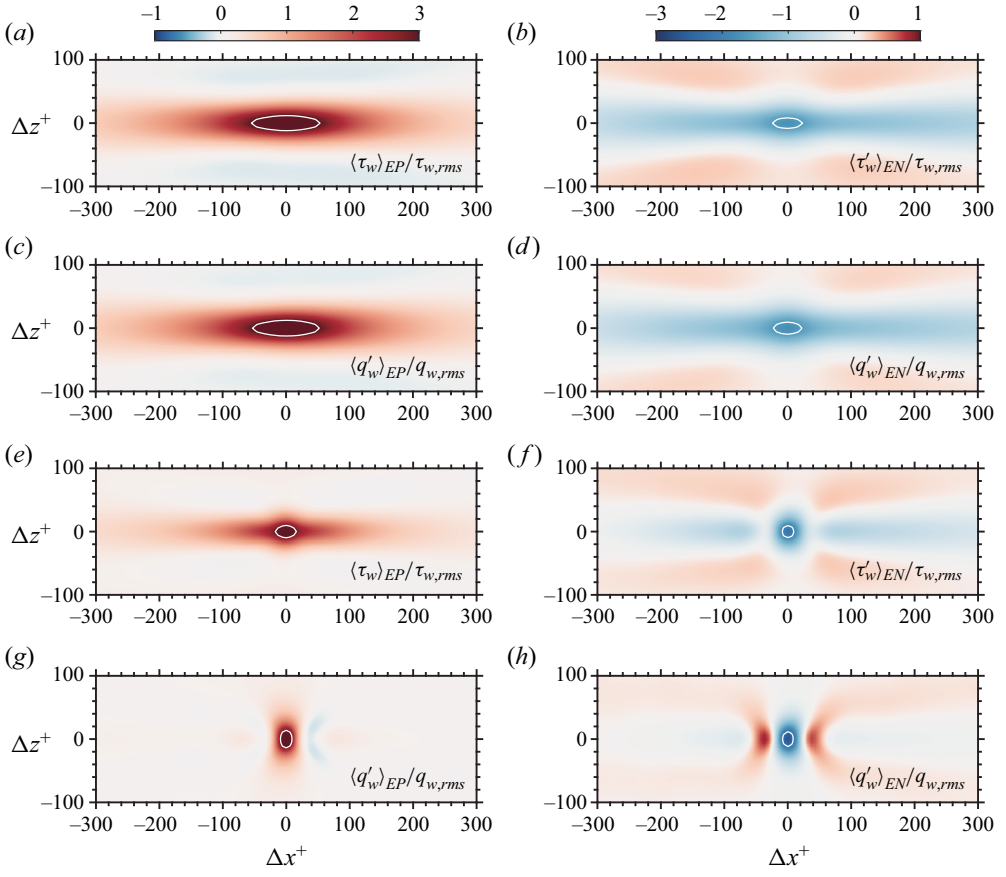

Figure 8. Conditionally averaged $\langle\tau'_w\rangle$ and $\langle q'_w\rangle$ fields around extreme events at $\Delta x^+ = 0$ and $\Delta z^+ = 0$ of (*a–d*) M2T05 and (*e–h*) M8T05. The left and right panels stand for EP and EN events, respectively. The white lines circle the regions belonging to extreme WSS and WHF fluctuations.

τ'_w and q'_w events occupy the majority, resulting in the percentages of 86 % and 76 % for EP and EN events, respectively. These percentages indicate that the same flow structures, i.e. near-wall streaks, play a dominating role in both extreme τ'_w and q'_w events. For M8T05, the overlapping percentages decrease significantly for EP events and slightly for EN events, suggesting there are different dominating flow structures associated with extreme τ'_w and q'_w events.

Conditionally averaged $\langle\tau'_w\rangle$ and $\langle q'_w\rangle$ fields in the vicinity of extreme events at $\Delta x^+ = 0$ and $\Delta z^+ = 0$ are plotted in figure 8, with the white lines circling the regions belonging to extreme WSS and WHF fluctuations. For M2T05, the $\langle\tau'_w\rangle$ and $\langle q'_w\rangle$ fields are similar to each other. Regarding EP events, the fluctuation patterns are of elongated shapes, and the extreme regions extend to a relatively large area. Regarding EN events, the areas of extreme regions are quite small, and high-value regions are observed at two sides. However, for M8T05, only in the $\langle\tau'_w\rangle_{EP}$ field is an elongated structure present. All of the extreme regions circled with white lines show spotty shapes. The streamwise structures in the $\langle\tau'_w\rangle_{EN}$ field seem to be split around the extreme region, with the centre structure extending in the spanwise direction. As far as the $\langle q'_w\rangle$ fields are concerned, the fine-scale alternating positive and negative patterns are shown, reminding us of the dominant role of APNSs in

the extreme events of q'_w. For the three-dimensional coherent structures associated with extreme events, they will be discussed in detail with a combination of the conditional skin-friction and heat-transfer decompositions in §§ 4.3 and 4.4.

4.2. *Conditional skin-friction and heat-transfer decompositions*

The skin-friction and heat-transfer decompositions based on integral identities are able to provide valuable insight into transport mechanisms contributing to WSS and WHF (Wenzel *et al.* 2022; Xu *et al.* 2022). Based on integrating the conservation laws of different quantities, such as momentum (Fukagata *et al.* 2002), mean kinetic energy (Renard & Deck 2016), mechanical energy (Drela 2009), total enthalpy (Wenzel *et al.* 2022), internal energy (Xu *et al.* 2022) and so on, there are many kinds of different integral identities. However, all these identities are based on overall averaged equations and are proposed to describe the mean flow and corresponding transport mechanisms; some transient behaviours, such as in extreme events of τ'_w and q'_w discussed here, cannot be taken into account in isolation yet. For depicting extreme events and demonstrating how coherent structures associated with extreme events contribute to τ'_w and q'_w, we have developed the conditional skin-friction and heat-transfer decompositions based on the conditionally averaged governing equations.

Referring to recently developed skin-friction and heat-transfer decompositions on mean flow (Wenzel *et al.* 2022; Xu *et al.* 2022), the FIK-like identity with twofold integration is adopted here, which owns a more intuitive physical interpretation of the underlying mechanisms of transferring momentum and energy than the RD and original FIK decompositions (Wenzel *et al.* 2022). We start from the fully compressible Navier–Stokes equations and use the conditional average on extreme events, so that the corresponding physical mechanisms associated with extreme τ'_w and q'_w can be particularly assessed. In combination with the continuity equation, the conditionally averaged streamwise-momentum equation can be written as

$$\langle\rho\rangle\frac{\partial\tilde{u}}{\partial t}+\langle\rho\rangle\tilde{u}_j\frac{\partial\tilde{u}}{\partial x_j}+\frac{\partial\,\langle\rho\rangle\,\widetilde{u''u''_j}}{\partial x_j}=-\frac{\partial\,\langle p\rangle}{\partial x}+\sqrt{\gamma}\frac{M}{Re}\frac{\partial\langle\tau_{1j}\rangle}{\partial x_j},\tag{4.1}$$

where the symbol $\widetilde{(\bullet)}$ denotes the conditional Favre average $\tilde{\phi}=\langle\rho\phi\rangle/\langle\rho\rangle$, the symbol $(\bullet)''$ denotes the fluctuation in the context of the conditional Favre average $\phi''=\phi-\tilde{\phi}$. Based on the FIK-like identity, the conditionally averaged skin-friction coefficient can be decomposed as

$$\left\langle C_f\right\rangle=C_f^M+C_f^T+C_f^P+C_f^B+C_f^U,\tag{4.2}$$

specifically,

$$C_f^M=-\frac{1}{q_\infty y_b}\int_0^{y_b}(y_b-y)\,\langle\rho\rangle\tilde{u}_j\frac{\partial\tilde{u}}{\partial x_j}\mathrm{d}y,\tag{4.3}$$

$$C_f^T=-\frac{1}{q_\infty y_b}\int_0^{y_b}(y_b-y)\left(\frac{\partial\langle\rho\rangle\widetilde{u''u''}}{\partial x}+\frac{\partial\langle\rho\rangle\widetilde{u''w''}}{\partial z}\right)+\langle\rho\rangle\widetilde{u''v''}\mathrm{d}y,\tag{4.4}$$

$$C_f^P=-\frac{1}{q_\infty y_b}\int_0^{y_b}(y_b-y)\frac{\partial\langle p\rangle}{\partial x}\mathrm{d}y,\tag{4.5}$$

$$C_f^B = \frac{1}{q_\infty y_b}\frac{\sqrt{\gamma}M}{Re}\int_0^{y_b}(y_b - y)\left(\frac{\partial\langle\tau_{xx}\rangle}{\partial x} + \frac{\partial\langle\tau_{xz}\rangle}{\partial z}\right) + \langle\tau_{xy}\rangle \mathrm{d}y, \tag{4.6}$$

$$C_f^U = -\frac{1}{q_\infty y_b}\int_0^{y_b}(y_b - y)\langle\rho\rangle\frac{\partial\tilde{u}}{\partial t}\mathrm{d}y, \tag{4.7}$$

where $q_\infty = \rho_\infty u_\infty^2/2$ is the dynamic pressure and y_b denotes the upper bound of integrals. According to the physical meanings of the integrands, each term can be interpreted as: C_f^M is the mean-convection term; C_f^T is the turbulent-convection term; C_f^P is the pressure-gradient term; C_f^B is the boundary-layer term and C_f^U is the unsteady term.

In the same way, based on the conditionally averaged internal energy equation

$$\langle\rho\rangle\frac{\partial\tilde{T}}{\partial t} + \langle\rho\rangle\tilde{u}_j\frac{\partial\tilde{T}}{\partial x_j} + \frac{\partial\langle\rho\rangle\widetilde{T''u_j''}}{\partial x_j} = -\frac{1}{c_v}\left\langle p\frac{\partial u_j}{\partial x_j}\right\rangle + \frac{\sqrt{\gamma}}{c_v}\frac{M}{Re}\left\langle\tau_{ij}\frac{\partial u_i}{\partial x_j}\right\rangle + \frac{1}{c_v\alpha}\frac{\partial}{\partial x_j}\left\langle\mu\frac{\partial T}{\partial x_j}\right\rangle, \tag{4.8}$$

the conditionally averaged heat-transfer coefficient can be decomposed as

$$\langle C_h\rangle = C_h^M + C_h^T + C_h^P + C_h^V + C_h^B + C_h^U, \tag{4.9}$$

specifically,

$$C_h^M = -\frac{c_v}{\beta y_b}\int_0^{y_b}(y_b - y)\langle\rho\rangle\tilde{u}_j\frac{\partial\tilde{T}}{\partial x_j}\mathrm{d}y, \tag{4.10}$$

$$C_h^T = -\frac{c_v}{\beta y_b}\int_0^{y_b}(y_b - y)\left(\frac{\partial\langle\rho\rangle\widetilde{T''u''}}{\partial x} + \frac{\partial\langle\rho\rangle\widetilde{T''w''}}{\partial z}\right) + \langle\rho\rangle\widetilde{T''v''}\mathrm{d}y, \tag{4.11}$$

$$C_h^P = -\frac{1}{\beta y_b}\int_0^{y_b}(y_b - y)\left\langle p\frac{\partial u_j}{\partial x_j}\right\rangle\mathrm{d}y, \tag{4.12}$$

$$C_h^V = \frac{1}{\beta y_b}\frac{\sqrt{\gamma}M}{Re}\int_0^{y_b}(y_b - y)\left\langle\tau_{ij}\frac{\partial u_i}{\partial x_j}\right\rangle\mathrm{d}y, \tag{4.13}$$

$$C_h^B = \frac{c_v}{\beta y_b}\frac{1}{c_v\alpha}\int_0^{y_b}(y_b - y)\left(\frac{\partial}{\partial x}\left\langle\mu\frac{\partial T}{\partial x}\right\rangle + \frac{\partial}{\partial z}\left\langle\mu\frac{\partial T}{\partial z}\right\rangle\right) + \left\langle\mu\frac{\partial T}{\partial y}\right\rangle\mathrm{d}y, \tag{4.14}$$

$$C_h^U = -\frac{c_v}{\beta y_b}\int_0^{y_b}(y_b - y)\langle\rho\rangle\frac{\partial\tilde{T}}{\partial t}\mathrm{d}y, \tag{4.15}$$

where the parameter β is defined as $\beta = \rho_\infty u_\infty c_p(T_r - T_w)$. Similarly, each term can be interpreted according to the physical meanings of the integrands as: C_h^M is the mean-convection term; C_h^T is the turbulent-convection term; C_h^P is the pressure-dilatation term; C_h^V is the viscous-dissipation term; C_h^B is the boundary-layer term and C_h^U is the unsteady term. The detailed derivations of the conditional skin-friction and heat-transfer decompositions are given in Appendix B. Note that compared with the conventional skin-friction and heat-transfer decomposition based on spanwise homogeneous and mean flow (Wenzel *et al.* 2022; Xu *et al.* 2022), the main differences are that some spanwise-gradient terms and unsteady terms are still retained in the present decompositions. Particularly, the accuracy of the conditional skin-friction and heat-transfer decompositions has been verified in Appendix C.

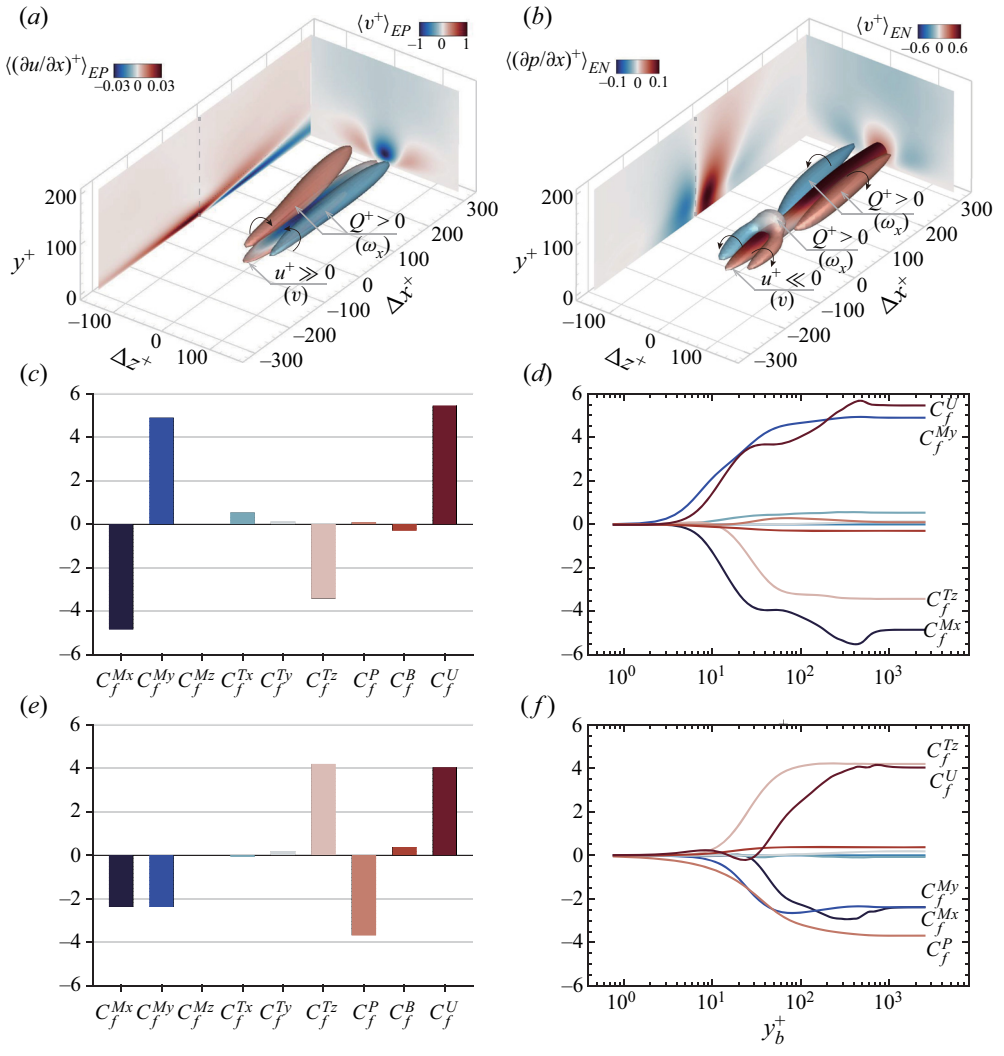

Figure 9. Conditional analysis on extreme events of τ_w' for M2T05: (*a*,*b*) conditionally averaged fluctuation fields, the isosurfaces of high-/low-speed streaks are flooded by v, the vortices displayed by the isosurfaces of Q-criterion are flooded by ω_x. An x–y plane at $\Delta z^+ = 0$ and a y–z plane at $\Delta x^+ = 0$ are shifted aside for clearer observation. Components of conditionally averaged skin-friction coefficients normalized by C_f: (*c*,*e*) C_f^i; (*d*,*f*) $C_f^i(y_b)$ as a function of the upper bound of integrals. Panels (*a*,*c*,*d*) and (*b*,*e*,*f*) are for the EP and EN events, respectively.

4.3. *Conditional analysis on extreme events of wall shear stress*

In this subsection, the above-introduced volumetric conditionally averaged fluctuation fields, in combination with the proposed decomposition identities, are used to analyse the coherent structures and their corresponding momentum and energy transport mechanisms in extreme events. Figure 9 shows the conditional analysis results on extreme τ_w' events for M2T05. In figure 9(*a*), a pair of energetic counter-rotating quasi-streamwise vortices is identified by the isosurface of Q-criterion coloured by the streamwise vorticity ω_x. These vortices induce strong sweep motions that facilitate high-speed flow from the outer layer to the inner layer. Consequently, a high-speed streak shown by the isosurface of $u^+ = 2.5$ coloured by the wall-normal velocity v is centred between the counter-rotating

vortices near the wall. This isosurface evolves from thin to wide and to thin again along the streamwise direction, which indicates the local streamwise velocity gradient changes from positive to negative, as shown in the x–y plane shifted from $\Delta z^+ = 0$. In the view of quadrant analysis (Wallace 2016), these structures associated with EP events of τ_w' induce a strong Q4 event. This flow topology is consistent with those observed in the incompressible TBL (Pan & Kwon 2018), pipe flow (Guerrero *et al.* 2020) and compressible TBL (Tong *et al.* 2022). These identified coherent structures are also consistent with the conceptual model proposed by Guerrero *et al.* (2020). Due to the orientation of rotation, it can be deduced that the counter-rotating vortex pair is composed of the legs of two individual spanwise-arranged hairpin-like vortices, which are widely present in wall-bounded turbulent flows.

The components of conditionally decomposed skin-friction coefficients normalized by C_f are displayed in figure 9(c,e). First, the present sample numbers of extreme events used for decompositions are sufficient to achieve statistical convergence, which has been proved in Appendix D. For a detailed comparison, the components of the mean-convection term C_f^M and the turbulent-convection term C_f^T in three directions are shown. The legend of lines in figure 9(d,f) can refer to figure 9(c,e) in which the colour correspondences are the same. As indicated in figure 9(d), $C_f^i(y_b)$ are independent on the integral upper bounds when $y_b^+ > 800$, within which the choice of y_b does not affect the integral results. The dominating terms are the streamwise mean-convection term C_f^{Mx}, wall-normal mean-convection term C_f^{My}, spanwise turbulent-convection term C_f^{Tz} and unsteady term C_f^U, whose magnitudes reach several times that of C_f. Due to the streamwise evolving of the high-speed streak, the near-wall streamwise velocity gradient has a large positive value, producing the coefficient C_f^{Mx} of a large negative integral value. Moreover, it is worth noting that the profile of C_f^U seems to be similar to that of C_f^{Mx} but with an opposite sign. Provided with Taylor's frozen-flow model and assuming that the flow is streamwise dominated, it is possible to derive $\partial\tilde{u}/\partial t = -u_c\partial\tilde{u}/\partial x$ with u_c being the convection velocity. If the convection velocity u_c satisfies $u_c = \tilde{u}$, the profiles of C_f^{Mx} and C_f^U are expected to be opposite to each other. Actually, the convection velocity is found to be consistent with the mean velocity except for very near the wall (Zhao & He 2009; Zhang, Wan & Sun 2019). Eventually, the similar profiles of C_f^{Mx} and C_f^U could be achieved. The strong sweep motions (Q4) are the key reason to induce the EP events of τ_w', which transfer amounts of momentum from the outer layer to the inner layer. The large-magnitude negative $\tilde{v}$ produces the coefficient C_f^{My} of a large positive integral value. In addition, the location of EP events is between the spanwise arranged energetic vortex pairs, and the coherent vortex pair in a counter-rotating state can induce strong spanwise turbulent fluctuations. Thus, as a result of the large gradient of Reynolds stress $\widetilde{u''w''}$ in the spanwise, the coefficient C_f^{Tz} also becomes an important component.

The coherent structures associated with the EN events of τ_w' are shown in figure 9(b). A hairpin-like vortex following a pair of counter-rotating quasi-streamwise vortices is identified. The pair of counter-rotating vortices could also be regarded as two legs of a hairpin-like vortex. The rotating directions of the vortex pair are opposite to those in the EP events. An elongated low-speed streak is centred between the counter-rotating quasi-streamwise vortices, sustained by strong ejecting motions induced by these vortices. Therefore, the region of the streak which is shown by the isosurface of $u^+ = -3$ is under

a Q2 event. These identified coherent structures associated with the EN events also agree with the conceptual models proposed by Sheng *et al.* (2009) and Guerrero *et al.* (2020). The extreme events tend to be located under the two continuously streamwise-arranged hairpin-like vortices. The dominating terms are partly the same as the terms of EP events: the streamwise mean-convection term C_f^{Mx}, wall-normal mean-convection term C_f^{My}, spanwise turbulent-convection term C_f^{Tz} and unsteady term C_f^{U}. Notably, an additional dominating term is the pressure-gradient term C_f^{P}. Due to the opposite rotating direction and the difference between high- and low-speed streaks, the contributions of C_f^{My} and C_f^{Tz} for EN events are quantitatively opposite to their contributions for EP events. Eventually, the mechanism which contributes most to the EN events is the pressure-gradient term C_f^{P}. The two-part structures of coherent vortices are probably related to the convecting pressure wavepackets as shown in the shifted x–y plane. The extreme events are located behind the wave valley, resulting in a large negative value of C_f^{P}.

As for coherent structures associated with the EP events of τ_w' for M8T05 shown in figure 10(a), the structures are partly similar to the counterparts of M2T05. The energetic counter-rotating quasi-streamwise vortex pair and the high-speed streak centring between the vortex pair are also identified. The biggest difference is that a spanwise-extending bridge vortex located at the EP events connects the vortex pair. This vortex is related to dilatation motions, because it is induced by the upstream expansion and downstream compression motions shown by the isosurface of $\theta^+ = \pm 0.02$. These alternating negative and positive dilatational motions remind us of the presence of APNSs in M8T05 which tend to be embedded in streaks. Despite the slight increasing contribution of other terms, the dominating terms are the same as those in M2T05: the streamwise mean-convection term C_f^{Mx}, wall-normal mean-convection term C_f^{My}, spanwise turbulent-convection term C_f^{Tz} and unsteady term C_f^{U}. The contributions of C_f^{My} and C_f^{Tz} are qualitatively in agreement with those in M2T05, because of the similar counter-rotating quasi-streamwise vortex pair. Due to the strong sweep motion at EP events, the momentum is transferred from the outer layer to the inner layer, and C_f^{My} contributes most to extreme τ_w'. Here, C_f^{Mx} and C_f^{U} show opposite contributions compared to those in M2T05, resulting from the deceleration region located at the buffer and log layer, but the sum of their contributions is still small.

The coherent structures associated with the EN events shown in figure 10(b) become more complex. A horseshoe-like vortex is located behind the EN event, and the two legs are also in a counter-rotating state. A brush-shaped low-speed elongated streak is above the EN events sustained by ejection motions, indicating that EN events of τ_w' for M8T05 are also related to the Q2 event. A similar spanwise-extending vortex is located at the EN events, and it is also induced by strong dilatation motions. However, in contrast to the EP event, the vortex is caught by upstream compression and downstream expansion motions shown by the isosurface of $\theta^+ = \pm 0.04$. The dominating terms are only the streamwise mean-convection term C_f^{Mx}, wall-normal mean-convection term C_f^{My} and unsteady term C_f^{U}. The magnitudes of these terms are relatively large, and C_f^{U} even reaches nearly $20C_f$. Comparing the coherent structures in other extreme events, we find that there is no quasi-streamwise vortex pair near the EN event; thus, the contribution of the spanwise turbulent-convection term C_f^{Tz} becomes much less important. On account of the acceleration in the buffer and log layers, the streamwise mean-convection term

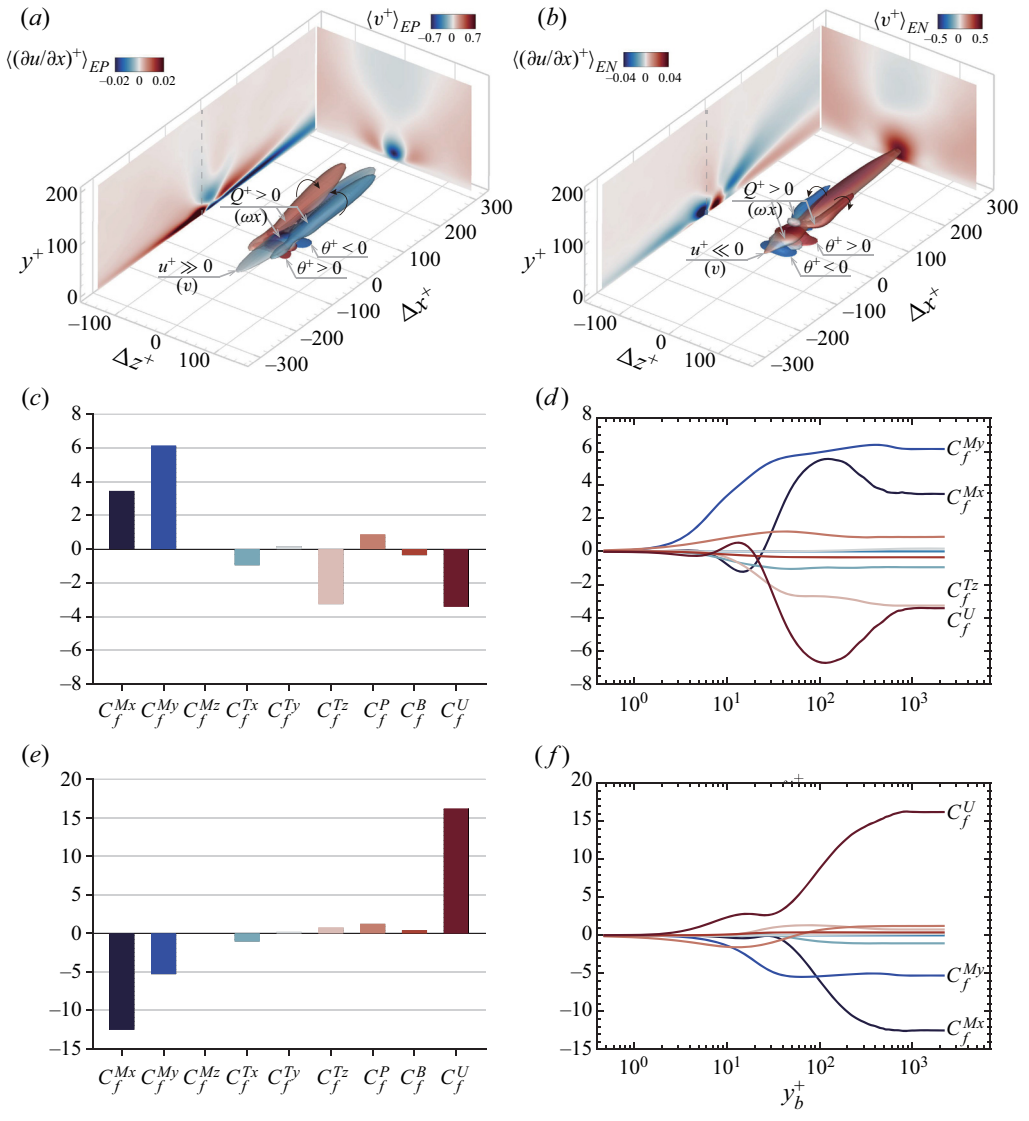

Figure 10. Conditional analysis on extreme events of τ_w' for M8T05: (*a*,*b*) conditionally averaged fluctuation fields, the isosurfaces of dilatation θ^+ are flooded by itself, the isosurfaces of high-/low-speed streaks are flooded by v, the vortices displayed by the isosurfaces Q-criterion are flooded by ω_x. An x–y plane at $\Delta z^+ = 0$ and a y–z plane at $\Delta x^+ = 0$ are shifted aside for clearer observation. Components of conditionally averaged skin-friction coefficients normalized by C_f: (*c*,*e*) C_f^i; (*d*,*f*) $C_f^i(y_b)$ as a function of upper bound of integrals. Panels (*a*,*c*,*d*) and (*b*,*e*,*f*) are for the EP and EN events, respectively.

C_f^{Mx} contributes to the EN events the most. This also suggests the correlation between the outer-layer large-scale structures and the inner-layer small-scale APNS. Meanwhile, the Q2 event induces momentum transport from the inner layer to the outer layer by wall-normal mean-convection C_f^{My}. These coherent structures make C_f^U a dominating term to balance the contributions of C_f^{Mx} and C_f^{My}.

Due to the co-existence of strong shear and dilatation motions, the coherent structures associated with extreme events of τ_w' for M8T05 tend to be more complex than those for

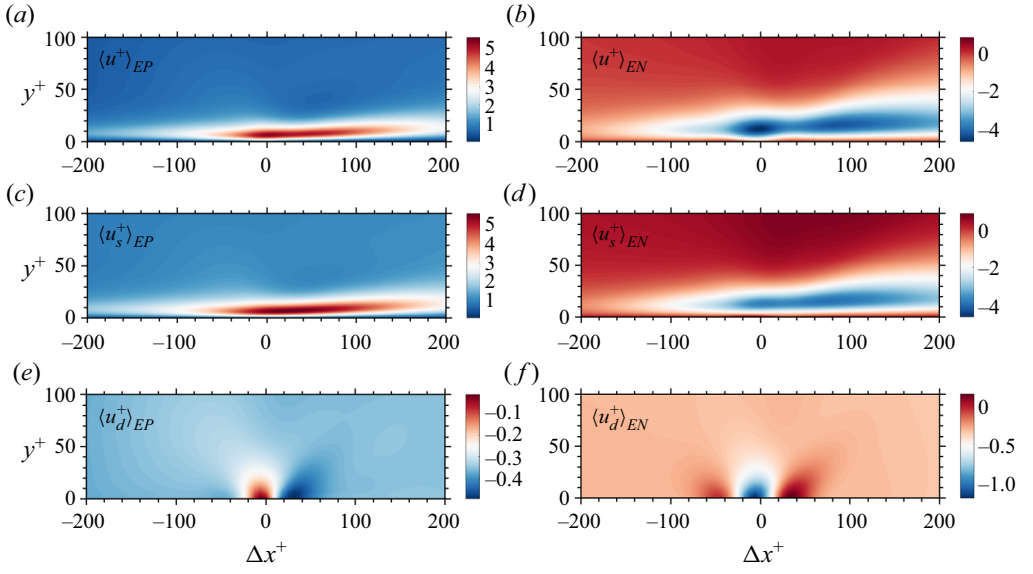

Figure 11. Contours of the conditionally averaged fluctuation field of extreme τ_w' events for M8T05 at $\Delta z^+ = 0$ plane: (*a*,*b*) the streamwise velocity u; (*c*,*d*) the solenoidal component u_s and (*d*,*f*) the dilatational component u_d. Panels (*a*,*c*,*e*) and (*b*,*d*,*f*) are for EP and EN events, respectively.

M2T05. To disentangle the coupled contributions of shear and dilatational motions, we perform the Helmholtz decomposition to cast the velocity $\boldsymbol{u}$ as the sum of a solenoidal part $\boldsymbol{u}_s$ and an irrotational part $\boldsymbol{u}_d$, which satisfy $\boldsymbol{\nabla}\cdot\boldsymbol{u}_s = 0$ and $\boldsymbol{\nabla}\times\boldsymbol{u}_d = 0$, respectively. Based on the velocity field $\boldsymbol{u}$, these two parts can be obtained by solving Poisson equations of the vector potential $\boldsymbol{A}$ and scalar potential φ:

$$\nabla^2\boldsymbol{A} = -\boldsymbol{\nabla}\times\boldsymbol{u}, \quad \nabla^2\varphi = \boldsymbol{\nabla}\cdot\boldsymbol{u}. \tag{4.16a,b}$$

Subsequently, the solenoidal and dilatational components can be calculated by

$$\boldsymbol{u}_s = \boldsymbol{\nabla}\times\boldsymbol{A}, \quad \boldsymbol{u}_d = \boldsymbol{\nabla}\varphi. \tag{4.17a,b}$$

Complemented with the boundary conditions (Hirasaki & Hellums 1970)

$$\frac{\partial\varphi}{\partial y} = 0, \quad \frac{\partial A_y}{\partial y} = 0, \quad A_x = A_z = 0, \tag{4.18a–c}$$

the vector potential $\boldsymbol{A}$ is shown to be unique. Figure 11(*a*) shows the $\langle u\rangle_{EP}$ field at the $\Delta z^+ = 0$ plane, with an elongated high-speed region locating near the wall. After the Helmholtz decomposition, the structures are clearly found to be composed of the high-speed streak exhibited in figure 11(*c*) by the solenoidal component $\langle u_s\rangle_{EP}$ and the APNSs exhibited in figure 11(*e*) by the dilatational component $\langle u_d\rangle_{EP}$. The high-speed streak denoted by $\langle u_s\rangle_{EP}$ is consistent with the original coherent structures observed in incompressible pipe flow (Guerrero *et al.* 2020) and supersonic TBL (Tong *et al.* 2022) in the EP event of τ_w'; thus, the APNSs denoted by $\langle u_d\rangle_{EP}$ are additional structures caused by the compressible effects in high-Mach-number flow. Nonetheless, the magnitude of APNSs is an order of magnitude smaller than that of the high-speed streak. As for EN events, similarly and more apparently, the structures are also composed of the low-speed streak exhibited in figure 11(*d*) by $\langle u_s\rangle_{EN}$ and the APNSs exhibited in figure 11(*f*)

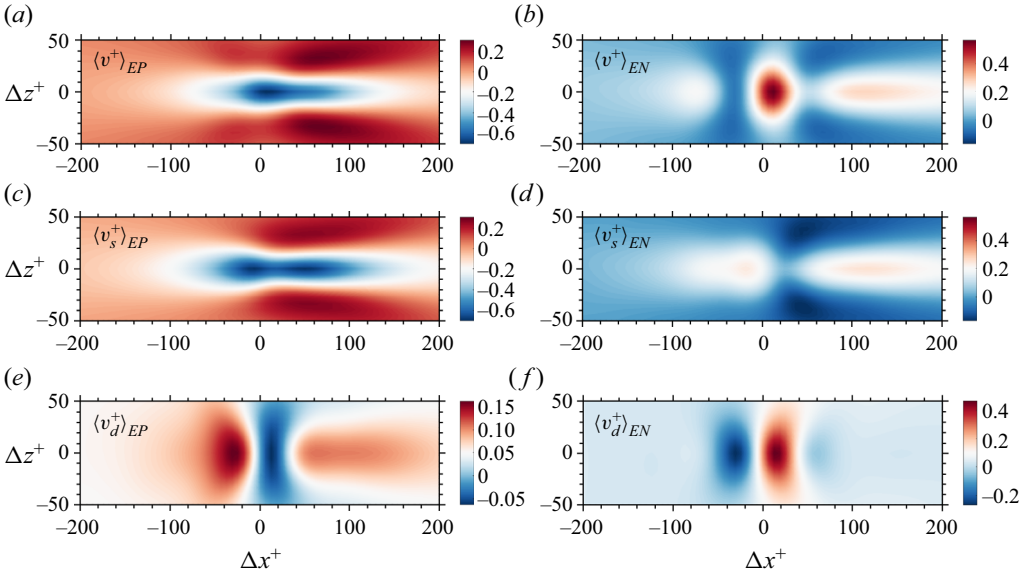

Figure 12. Contours of the conditionally averaged field based on extreme τ_w' events for M8T05 at the $y^+ = 15$ plane: (a,b) the wall-normal velocity v; (c,d) the solenoidal component v_s; (e,f) the dilatational component v_d. Panels (a,c,e) and (b,d,f) are for EP and EN events, respectively.

by $\langle u_d\rangle_{EN}$. The difference is that the low-speed streak is thicker in the wall-normal direction, and the magnitude of the APNSs becomes larger, which is comparable to the magnitude of the streak. The phases of APNSs are reversed in EN and EP events, implying that EP or EN events are related to opposite dilatational motions.

To illustrate the ejection and sweep motions induced by these two structures, figure 12 shows contours of conditionally averaged wall-normal velocity at the $y^+ = 15$ plane. The strong sweep motion is observed near the location of extreme events in figure 12(a). The streak pattern in the $\langle v_s\rangle_{EP}$ field shown in figure 12(c) is more well shaped and extends longer than that in figure 12(a). Two ejecting regions simultaneously induced by the quasi-streamwise vortex pair flank the central sweeping region. The $\langle v_d\rangle_{EP}$ field in figure 12(e) shows the appearance of APNSs also with a relatively small magnitude. As for EN events, the structures in the $\langle v\rangle_{EP}$ field shown in figure 12(b) are split into several parts by weak and strong ejection motions along the x direction, which consist of local ejection spots and elongated streaks. In the $\langle v_s\rangle_{EN}$ field shown in figure 12(d), the upstream ejection streak shrinks at $\Delta x^+ \approx 15$ first, and then grows to be elongated. In the $\langle v_d\rangle_{EN}$ field shown in figure 12(f), the strong APNSs are identified, resulting in streamwise alternating sweeping and ejection motions. The spanwise and streamwise length scales of APNSs are consistent with the characteristic wavelength of the inner peak in figure 7(c). The APNSs also enhance ejection motions at the location of EN events. Moreover, there are phase differences in APNSs between the u_d field and v_d field. Similarly, Yu *et al.* (2019) performed Helmholtz decomposition to study compressibility effects on skin friction in turbulent channel flow. Through a modified FIK decomposition, they found a relatively small contribution of dilatational component $\boldsymbol{u}_d$ (approximately 4 %) to the overall skin-friction coefficient C_f in the cooled channel flow of a bulk Mach number $M_b = 4.4$ with the presence of APNSs. However, the dilatational component $\boldsymbol{u}_d$ plays a much more important role in extreme τ_w' events.

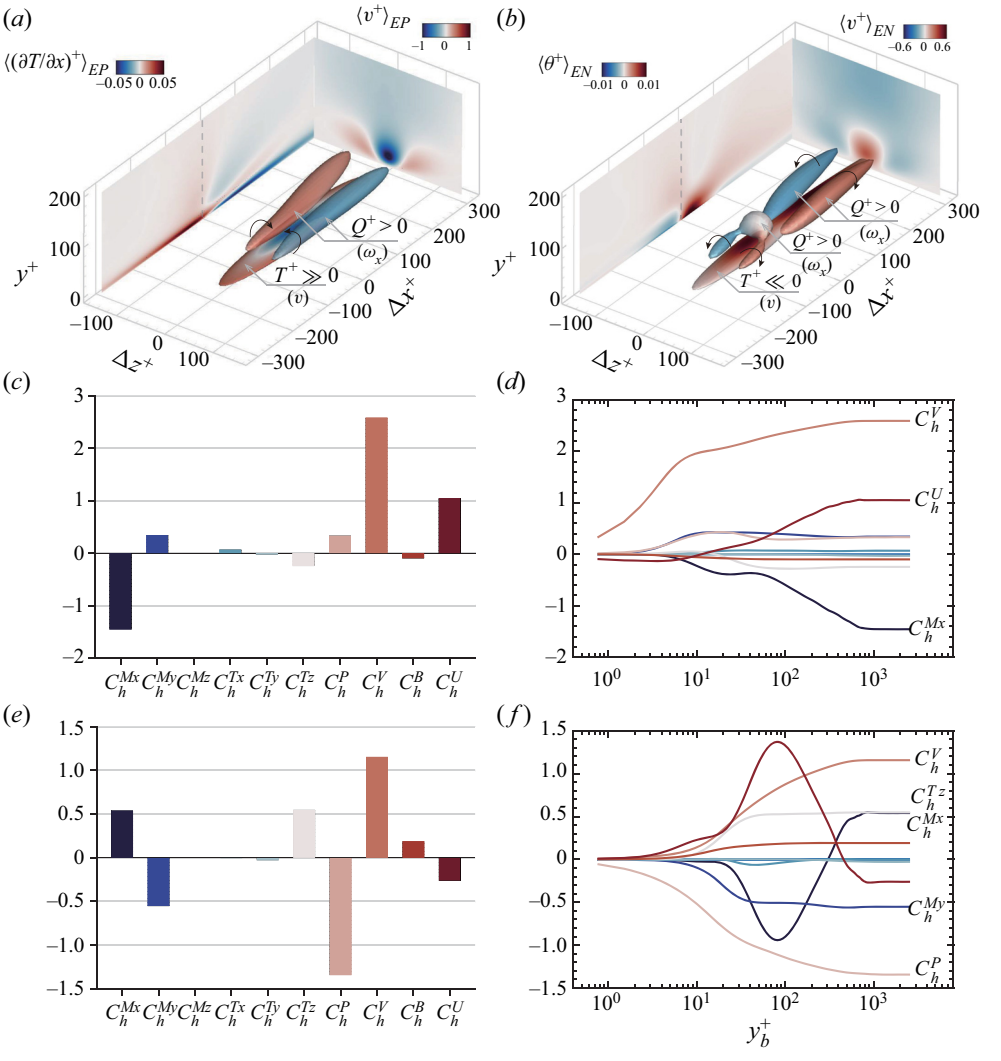

Figure 13. Conditional analysis on extreme events of q'_w for M2T05: (*a*,*b*) conditionally averaged fluctuation fields, the isosurfaces of high-/low-temperature streaks are flooded by v, the vortices displayed by the isosurfaces of Q-criterion are flooded by ω_x. An x–y plane at $\Delta z^+ = 0$ and a y–z plane at $\Delta x^+ = 0$ are shifted aside for clearer observation. Components of conditionally averaged heat-transfer coefficients normalized by C_h: (*c*,*e*) C_h^i; (*d*,*f*) $C_h^i(y_b)$ as a function of the upper bound of integrals. Panels (*a*,*c*,*d*) and (*b*,*e*,*f*) are for the EP and EN events, respectively.

4.4. *Conditional analysis on extreme events of wall heat flux*

Similarly, extreme q'_w events are analysed in the same framework. According to the joint p.d.f. in figure 5(*b*) where the q'_w is nearly linearly positively correlated with the τ'_w, the extreme events of τ'_w and q'_w are mostly overlapped with each other for M2T05 referring to the overlapping percentages in table 5. Thus, the coherent structures associated with the EP events of q'_w shown in figure 13(*a*) are quite similar to those of τ'_w shown in figure 9(*a*). A high-temperature elongated streak shown by the isosurface of $T^+ = 4$ centring between the counter-rotating quasi-streamwise vortex pair is subjected to sweep motions. The isosurface of this high-temperature streak evolves from thin to wide and

to thin again along the streamwise direction, which indicates that the local streamwise temperature gradient changes from positive to negative as shown in the x–y plane shifted from $\Delta z^+ = 0$. The dominating contributing terms are the streamwise mean-convection term C_f^{Mx}, the viscous-dissipation term C_h^V and the unsteady term C_f^U. The counter-rotating vortex pair inducing sweep motions enhances the near-wall shear $\partial u/\partial y$, thus the EP event of q_w' for M2T05 is mainly the result of strong molecular viscous heating within the viscous sublayer ($y^+ < 5$).

For the EN event of q_w', the coherent structures shown in figure 13(b) are also similar to those of τ_w' shown in figure 9(b). A hairpin-like vortex following a pair of counter-rotating quasi-streamwise vortices is identified, and an elongated low-temperature streak shown by the isosurface of $T^+ = -4$ centres between these vortices. Under these coherent structures, there is no very dominant term as the streamwise mean-convection term C_f^{Mx}, the wall-normal mean-convection term C_f^{My}, the spanwise turbulent-convection term C_f^{Tz}, the viscous-dissipation term C_h^V, the pressure-dilatation term C_h^P and the unsteady term C_f^U all have relatively considerable contributions. Compared with the dominating terms of EP events, the magnitudes of these terms of EN events are relatively small. The near-wall molecular viscous heating is highly mitigated. As is shown in the x–y plane shifted from $\Delta z^+ = 0$, streamwise extended compression and expansion motions are located near the EN event, which could be related to the convecting wavepackets within the boundary layer; thus the most important transport mechanism of energy contributing to EN events becomes the pressure-dilatation work C_h^P.

The scenario in extreme events of q_w' for M8T05 is quite different. The coherent structures associated with extreme events shown in figure 14(a,b) are formed by local fine-scale spanwise-extending spotty structures near the wall, without the presence of the elongated velocity/temperature streaks and counter-rotating quasi-streamwise vortex pair observed in other extreme events. Intuitively, these dilational spanwise-extending spotty structures correspond to the APNSs directly observed in figure 6(d). The length scale of these structures is also consistent with the corresponding wavelength of the dominant spectral peak in figure 7(d). For the EP event, a fine-scale spanwise extending vortex with negative spanwise vorticity ($\omega_z < 0$) is induced by the upstream expansion and downstream compression shown by isosurfaces of $\theta^+ = \pm 0.07$, respectively. The EP events are favourable to occur behind the inflection points of APNSs where expansion transitions to compression. A vortex sheet with ($\omega_z > 0$) off the wall in the buffer layer is located downstream of the EP event. The high-temperature region of $T^+ = 2$ becomes a tiny isolated wall-mounted spot at the location of EP events. The dominant energy transport mechanisms seem to be much simpler than those in M2T05, the streamwise convection of the strong APNSs dominates due to their feature of convecting wavepackets. Meanwhile, the contribution of pressure-dilatation work C_h^P is comparable to that of molecular viscous heating C_h^V. The mean-convection term C_h^{Mx} and the unsteady term C_h^U are overwhelming on other terms and comparable to each other. Their magnitudes are very large, and can even exceed $60C_h$.

For the EN event, the coherent structures are also mainly associated with the APNSs. Compared with the EP event, the signs of the spanwise vorticity of the identified vortex and the dilatation are inverse, namely a fine-scale spanwise-extending near-wall vortex with positive spanwise vorticity ($\omega_z > 0$) is induced by the upstream compression and downstream expansion shown by isosurfaces of $\theta^+ \pm 0.07$. The EN events are favourable to occur behind the inflection points of APNSs where compression transitions to expansion. The low-temperature regions of $T^+ = -3$ are shown to be two parts: one is

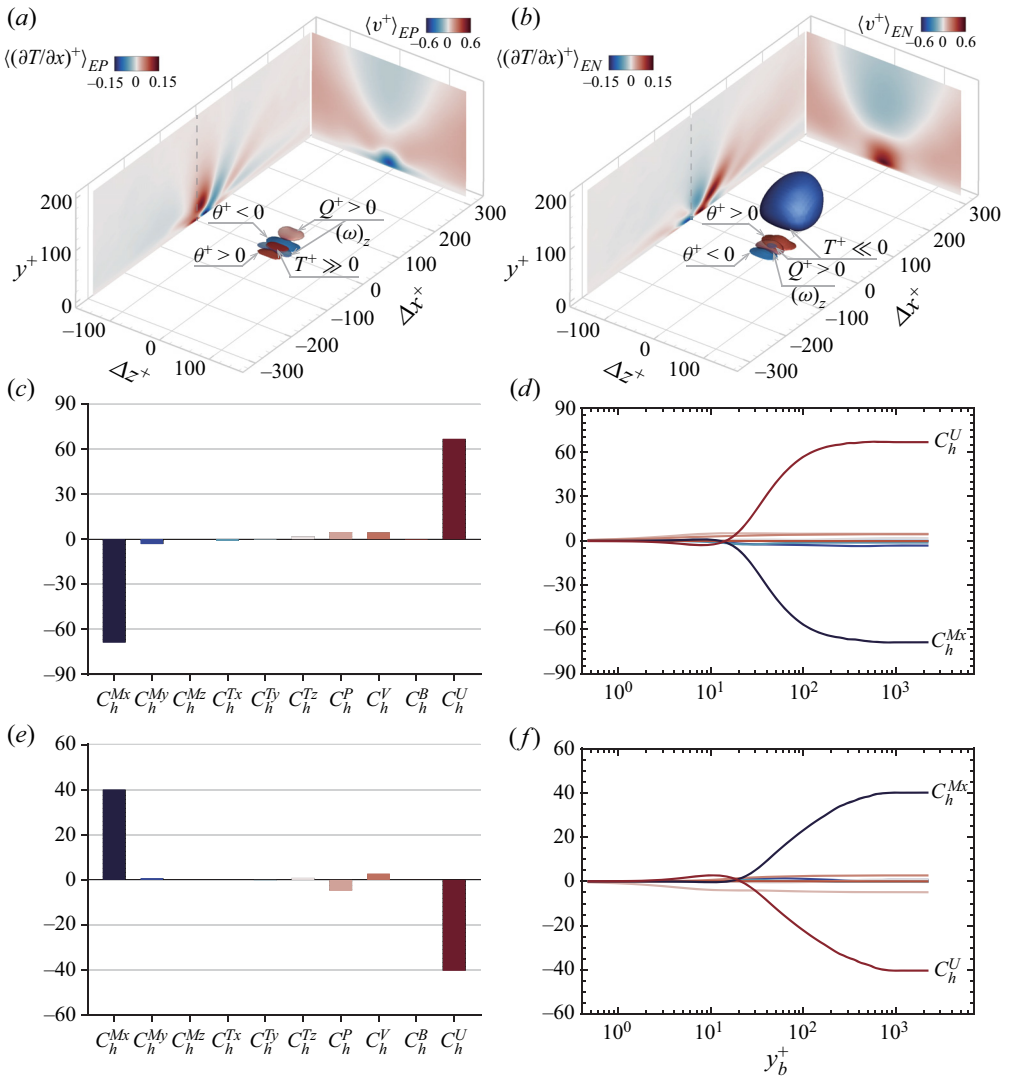

Figure 14. Conditional analysis on extreme events of q'_w for M8T05: (*a*,*b*) conditionally averaged fluctuation fields, the isosurfaces of dilatation θ^+ and temperature T^+ are flooded by themselves, the vortices displayed by the Q-criterion are flooded by ω_z. An x–y plane at $\Delta z^+ = 0$ and a y–z plane at $\Delta x^+ = 0$ are shifted aside for clearer observation. Components of conditionally averaged heat-transfer coefficients normalized by C_h: (*c*,*e*) C_h^i; (*d*,*f*) $C_h^i(y_b)$ as a function of the upper bound of integrals. Panels (*a*,*c*,*d*) and (*b*,*e*,*f*) are for the EP and EN events, respectively.

also a tiny isolated wall-mounted spot at the location of EN events; another is a large-scale off-wall bubble. Similarly, the mean-convection term C_h^{Mx} and the unsteady term C_h^U are also overwhelming on other terms and comparable to each other. Compared with EP events, the growth of these two terms is slower persisting up to the wake, due to the low-temperature off-wall bubble. Meanwhile, the pressure-dilatation term C_h^P is also contributive to EN events.

Since the two terms C_h^{Mx} and C_h^U are overwhelming and almost cancel each other in both EP and EN events, to more clearly compare with other mechanisms, C_h^U and C_h^{Mx}

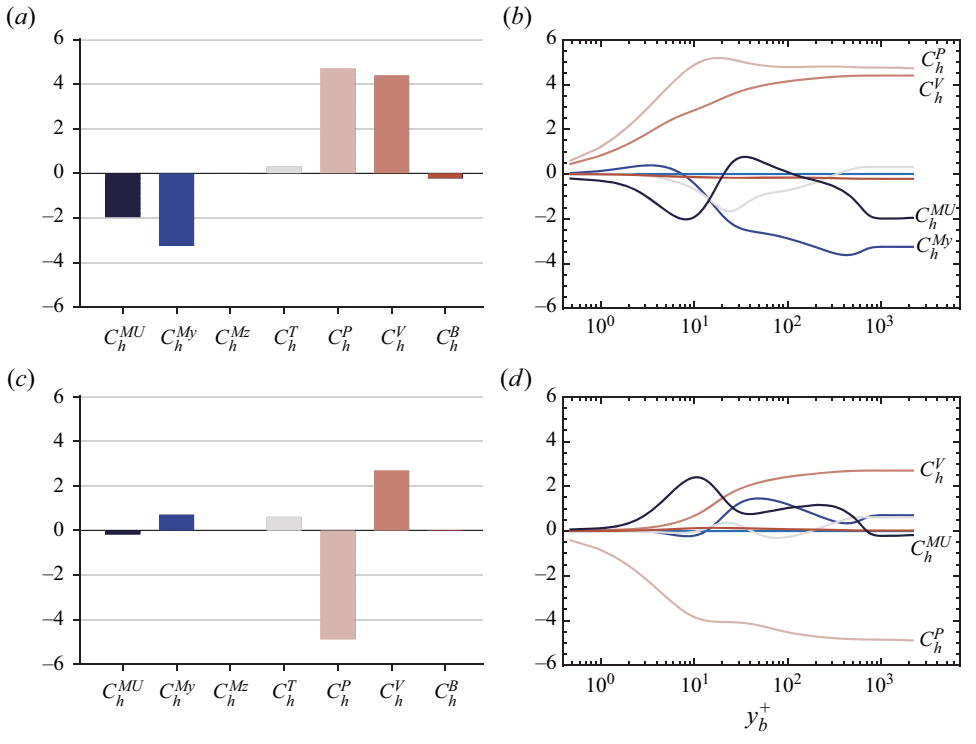

Figure 15. Recombined components of conditionally averaged heat-transfer coefficients for M8T05 normalized by C_h: (*a*,*c*) C_h^i; (*b*,*d*) $C_h^i(y_b)$ as a function of the upper bound of integrals. Panels (*a*,*b*) and (*c*,*d*) are for the EP and EN events, respectively.

are combined and denoted by $C_h^{MU} = C_h^{Mx} + C_h^U$, which is a measure of comprehensive contributions by convecting structures. As shown in figure 15, the magnitudes of the combined components C_h^{MU} become much smaller and comparable to other components. For EP events, the pressure-dilatation term C_h^P and viscous-dissipation term C_h^V play dominating roles, while C_h^V is expected to be always positive; and for EN events, the dominating contribution of C_h^P is highlighted. In this sense, the pressure-dilatation terms C_h^P, whose magnitudes grow rapidly near the wall ($y^+ < 10$), have the greatest contribution to both EP and EN events. These findings are consistent with the observations of the near-wall strong-dilatation structures APNSs in the conditionally averaged field.

5. Summary and conclusions

The extreme events of wall shear stress and heat flux in compressible TBLs are investigated by analysing DNS data. A supersonic case M2T05 and a hypersonic case M8T05 are considered to examine the effects of compressibility. The essential features of overall τ_w' and q_w' have been presented at first. In both TBLs, the distribution of skin-friction coefficient C_f versus Reynolds number Re_θ can be properly predicted by transformed Kármán–Schoenherr and Coles–Fernholz relations. The Reynolds analogy factors are seldom influenced by the Mach number, and the values of both cases are almost the same $s \approx 1.14$. Visually indicated by the fields of τ_w' and q_w', the primary structures associated with extreme events are high-/low-speed streaks in M2T05; in contrast, those in M8T05 become two types of distinct structures, i.e. the similar streaks and the unique

fine-scale APNSs. Correspondingly, only an individual peak emerges in the wavenumber spectra with relatively longer characteristic wavelength λ_x^+ for M2T05, while two distinct peaks corresponding to APNSs and streaks are observed in the spectra with separated characteristic wavelengths λ_x^+ for M8T05. Additionally, from τ_w' spectra to q_w' spectra, the dominating peak shifts from the peak of streaks to the peak of APNSs.

Second, the coherent structures associated with extreme events are identified by performing volumetric conditional average. In M2T05, the coherent structures involve organized hairpin-like vortices which can induce sweep/ejection events, but the conditional field becomes more complex in M8T05, and two types of coherent structures have been simultaneously identified, i.e. hairpin-like vortices and APNSs. Additionally, APNSs dominate the conditional field of extreme q_w' events for M8T05. Through Helmholtz decomposition, the natures of streaks and APNSs are shown to be related to solenoidal and dilatational motions, respectively. Furthermore, APNSs are found to be a type of structure capable of efficiently inducing extreme events of both τ_w' and q_w'.

Further, we propose the novel conditional skin-friction and heat-transfer decompositions based on a FIK-like identity that allows us to investigate the transport mechanisms of momentum and energy in extreme events quantitatively. The key features with respect to the transport mechanisms of these two types of coherent structures are clarified. For the hairpin-like vortices, the main transport mechanisms of momentum or energy are by the streamwise convection by speed/temperature streaks C_f^{Mx} or C_h^{Mx}, spanwise turbulent fluctuations C_f^{Tz} or C_h^{Tz}, and exchange of momentum or energy between the inner and outer layer by the sweep/ejection motions C_f^{My} or C_h^{My}. It is noteworthy that in the EN events, pressure-related terms, such as the pressure-gradient term C_f^P and the pressure-dilatation term C_h^P, are the primarily contributive terms. In contrast, for APNSs, the strong near-wall dilatational motions organized as convecting wavepackets dominate the transport of both momentum and energy by convection. Meanwhile, for energy transport, the pressure-dilatation work C_h^P becomes the most contributive mechanism, in contrast to the dominant role of viscous dissipation C_h^V in the viscous sublayer by the hairpin-like vortices. That is, in extreme events, the compressibility effects completely change the dominant transport mechanisms of energy by shifting the dominant flow process from transverse to longitudinal.

In short, it should be emphasized that the transport mechanisms of momentum and energy revealed above should be general since these identified streaks and APNSs are representative structures in compressible TBLs, even though the coherent structures associated with extreme events may depend on the parameters such as Mach number, temperature, etc. Of particular importance, this study offers a possible framework for analysing extreme events and corresponding transport mechanisms quantitatively by combining volumetric conditional average with the proposed conditional skin-friction and heat-transfer decompositions.

Acknowledgements. The numerical calculations in this paper were done using the supercomputing system in the Supercomputing Center of USTC. The authors thank the anonymous reviewers for their insightful suggestions.

Funding. This work was supported by the National Natural Science Foundation of China under grant nos. 92052301, 92252202, 12172351, 12322210 and 12388101, the China Postdoctoral Science Foundation 2022M723043, the Fundamental Research Funds for the Central Universities and the USTC Research Funds of the Double First-Class Initiative.

Declaration of interests. The authors report no conflict of interest.

Author ORCIDs.
Peng-Jun-Yi Zhang https://orcid.org/0000-0002-0554-9049;
Zhen-Hua Wan https://orcid.org/0000-0003-0035-3116;
Si-Wei Dong https://orcid.org/0000-0002-4725-2964;
Nan-Sheng Liu https://orcid.org/0000-0001-9128-1933;
Xi-Yun Lu https://orcid.org/0000-0002-0737-6460.

Appendix A. Governing equations of compressible Navier–Stokes equations

The fully compressible Navier–Stokes equations for perfect heat-conducting gas solved here are non-dimensionalized by the reference length L_∞, free stream density ρ_∞, scaled free stream acoustic velocity $c_\infty/\sqrt{\gamma}$, free stream temperature T_∞ and viscosity μ_∞ written as

$$\frac{\partial \rho}{\partial t} + \frac{\partial \rho u_i}{\partial x_i} = 0, \tag{A1a}$$

$$\frac{\partial \rho u_i}{\partial t} + \frac{\partial \rho u_i u_j}{\partial x_j} = -\frac{\partial p}{\partial x_i} + \sqrt{\gamma}\frac{M}{Re}\frac{\partial \tau_{ij}}{\partial x_j}, \tag{A1b}$$

$$\frac{\partial \rho E}{\partial t} + \frac{\partial \rho u_j H}{\partial x_j} = -\frac{1}{\alpha}\frac{\partial}{\partial x_j}\left(\mu\frac{\partial T}{\partial x_j}\right) + \sqrt{\gamma}\frac{M}{Re}\frac{\partial(\tau_{ij}u_i)}{\partial x_j}, \tag{A1c}$$

$$p = \rho T, \tag{A1d}$$

where ρ is the density, u_i is the velocity component in the ith direction ($i = 1, 2, 3$), p is the thermodynamic pressure, $E = c_v T + u_i u_i/2$ is the total energy per unit mass and $H = E + p/\rho$ is the total enthalpy. Here, τ_{ij} denotes the viscous stress tensor being

$$\tau_{ij} = \mu\left(\frac{\partial u_i}{\partial x_j} + \frac{\partial u_j}{\partial x_i} - \frac{2}{3}\frac{\partial u_k}{\partial x_k}\delta_{ij}\right). \tag{A2}$$

The dependence of the viscosity coefficient on temperature is determined by Sutherland's law. The non-dimensional governing parameters are the free stream Reynolds number $Re = \rho_\infty u_\infty L_\infty/\mu_\infty$, the Mach number $M = u_\infty/c_\infty$ and the Prandtl number $Pr = 0.72$.

Moreover, the governing equation of the internal energy can be expressed as

$$\frac{\partial \rho T}{\partial t} + \frac{\partial \rho T u_j}{\partial x_j} = -\frac{p}{c_v}\frac{\partial u_j}{\partial x_j} + \frac{\sqrt{\gamma}}{c_v}\frac{M}{Re}\tau_{ij}\frac{\partial u_i}{\partial x_j} + \frac{1}{c_v\alpha}\frac{\partial}{\partial x_j}\left(\mu\frac{\partial T}{\partial x_j}\right), \tag{A3}$$

where the parameter α is expressed as $1/\alpha = \sqrt{\gamma}c_p M/RePr$, with the specific heat ratio $\gamma = c_p/c_v = 1.4$.

Appendix B. Derivation of the conditional skin-friction and heat-transfer decompositions

Upon Cauchy's integral formula for repeated integration, n repeated integrations of a continuous function can be transformed to a single integral

$$\int_{y_l}^{y_b}\int_{y_l}^{y_2}\cdots\int_{y_l}^{y_{n-1}} f(y_n)\,\mathrm{d}y_n\cdots\mathrm{d}y_2\,\mathrm{d}y_1 = \frac{1}{(n-1)!}\int_{y_l}^{y_b}(y_b - y)^{n-1}f(y)\,\mathrm{d}y. \tag{B1}$$

In the present twofold repeated integration, n is chosen as $n = 2$. According to the non-slip boundary conditions at the wall, the gradient $\partial v/\partial x|_{y=0} = 0$ can be obtained. Performing

conditional average and integrating the wall-normal components of the viscous term in (4.1) and heat conduction term in (4.8) yields

$$\sqrt{\gamma}\frac{M}{Re}\int_0^{y_b}\int_0^{y}\frac{\partial}{\partial y}\left\langle\mu\left(\frac{\partial u}{\partial y}+\frac{\partial v}{\partial x}\right)\right\rangle \mathrm{d}y\,\mathrm{d}y$$
$$=\sqrt{\gamma}\frac{M}{Re}\int_0^{y_b}\left\langle\mu\left(\frac{\partial u}{\partial y}+\frac{\partial v}{\partial x}\right)\right\rangle-\left\langle\mu\frac{\partial u}{\partial y}\right\rangle\Big|_{y=0}\mathrm{d}y, \tag{B2}$$

$$\frac{1}{c_v\alpha}\int_0^{y_b}\int_0^{y}\frac{\partial}{\partial y}\left\langle\mu\frac{\partial T}{\partial y}\right\rangle\mathrm{d}y\,\mathrm{d}y=\frac{1}{c_v\alpha}\int_0^{y_b}\left\langle\mu\frac{\partial T}{\partial y}\right\rangle-\left\langle\mu\frac{\partial T}{\partial y}\right\rangle\Big|_{y=0}\mathrm{d}y. \tag{B3}$$

The conditional skin-friction and heat transfer coefficients are defined as

$$\langle C_f\rangle=\frac{\sqrt{\gamma}M}{q_\infty Re}\left\langle\mu\frac{\partial u}{\partial y}\right\rangle\Big|_{y=0},\quad \langle C_h\rangle=\frac{1}{\rho_\infty u_\infty c_p\alpha\,(T_r-T_w)}\left\langle\mu\frac{\partial T}{\partial y}\right\rangle\Big|_{y=0}, \tag{B4a,b}$$

where $q_\infty=\rho_\infty u_\infty^2/2$ is the dynamic pressure. By twofold repeated integration on (4.1) and (4.8), the integral identities of conditionally averaged skin-friction and heat-transfer coefficients are obtained

$$\langle C_f\rangle=\underbrace{-\frac{1}{q_\infty y_b}\int_0^{y_b}(y_b-y)\,\langle\rho\rangle\tilde{u}_j\frac{\partial\tilde{u}}{\partial x_j}\mathrm{d}y}_{C_f^M}\underbrace{-\frac{1}{q_\infty y_b}\int_0^{y_b}(y_b-y)\,\frac{\partial\langle p\rangle}{\partial x}\mathrm{d}y}_{C_f^P}$$
$$\underbrace{-\frac{1}{q_\infty y_b}\int_0^{y_b}(y_b-y)\left(\frac{\partial\langle\rho\rangle\widetilde{u''u''}}{\partial x}+\frac{\partial\langle\rho\rangle\widetilde{u''w''}}{\partial z}\right)+\langle\rho\rangle\widetilde{u''v''}\,\mathrm{d}y}_{C_f^T}$$
$$\underbrace{+\frac{1}{q_\infty y_b}\frac{\sqrt{\gamma}M}{Re}\int_0^{y_b}(y_b-y)\left(\frac{\partial\langle\tau_{xx}\rangle}{\partial x}+\frac{\partial\langle\tau_{xz}\rangle}{\partial z}\right)+\langle\tau_{xy}\rangle\,\mathrm{d}y}_{C_f^B}$$
$$\underbrace{-\frac{1}{q_\infty y_b}\int_0^{y_b}(y_b-y)\,\langle\rho\rangle\frac{\partial\tilde{u}}{\partial t}\mathrm{d}y}_{C_f^U}, \tag{B5}$$

$$\langle C_h\rangle=\underbrace{-\frac{c_v}{\beta y_b}\int_0^{y_b}(y_b-y)\,\langle\rho\rangle\tilde{u}_j\frac{\partial\tilde{T}}{\partial x_j}\mathrm{d}y}_{C_h^M}\underbrace{-\frac{1}{\beta y_b}\int_0^{y_b}(y_b-y)\left\langle p\frac{\partial u_j}{\partial x_j}\right\rangle\mathrm{d}y}_{C_h^P}$$
$$\underbrace{-\frac{c_v}{\beta y_b}\int_0^{y_b}(y_b-y)\left(\frac{\partial\langle\rho\rangle\widetilde{T''u''}}{\partial x}+\frac{\partial\langle\rho\rangle\widetilde{T''w''}}{\partial z}\right)+\langle\rho\rangle\widetilde{T''v''}\mathrm{d}y}_{C_h^T}$$

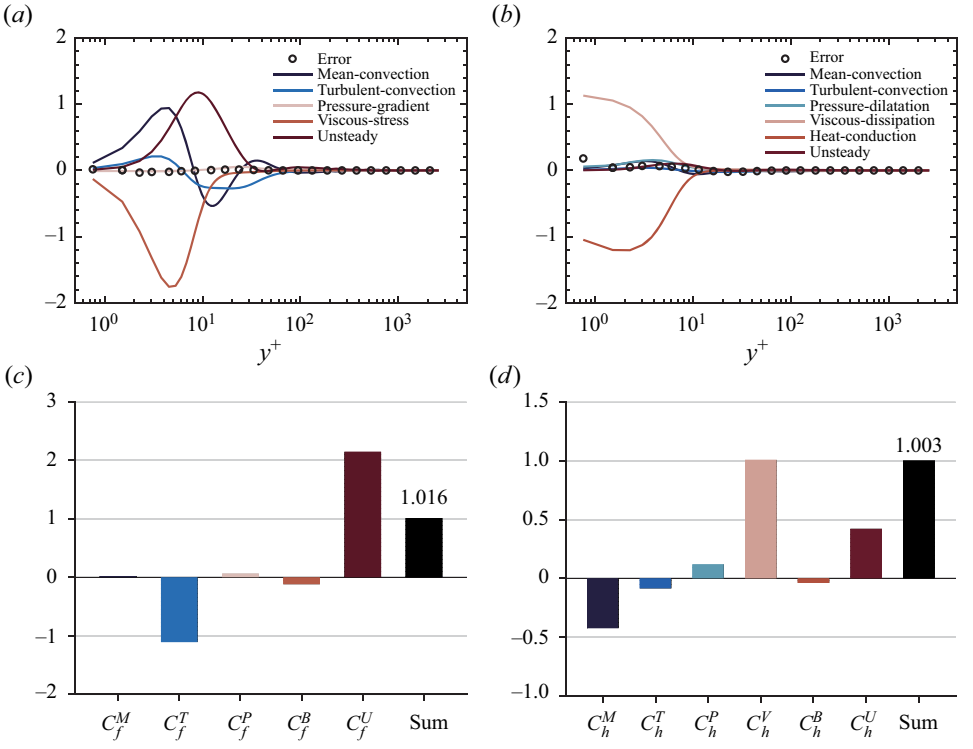

Figure 16. Budgets of conditionally averaged equations based on EP events of M2T05: (*a*) the momentum equation of (4.1) and (*b*) the energy equation of (4.8). Conditional decompositions: (*c*) components of conditionally averaged skin-friction coefficients C_f^i normalized by $\langle C_f\rangle_{EP}$; (*d*) components of conditionally averaged heat-transfer coefficients C_h^i normalized by $\langle C_h\rangle_{EP}$.

$$+\underbrace{\frac{c_v}{\beta y_b}\frac{1}{c_v\alpha}\int_0^{y_b}(y_b-y)\left(\frac{\partial}{\partial x}\left\langle\mu\frac{\partial T}{\partial x}\right\rangle+\frac{\partial}{\partial z}\left\langle\mu\frac{\partial T}{\partial z}\right\rangle\right)+\left\langle\mu\frac{\partial T}{\partial y}\right\rangle\mathrm{d}y}_{C_h^B}$$

$$+\underbrace{\frac{1}{\beta y_b}\frac{\sqrt{\gamma}M}{Re}\int_0^{y_b}(y_b-y)\left\langle\tau_{ij}\frac{\partial u_i}{\partial x_j}\right\rangle\mathrm{d}y}_{C_h^V}-\underbrace{\frac{c_v}{\beta y_b}\int_0^{y_b}(y_b-y)\langle\rho\rangle\frac{\partial\tilde{T}}{\partial t}\mathrm{d}y}_{C_h^U}, \tag{B6}$$

where y_b is the upper bound of integrals and the parameter $\beta=\rho_\infty u_\infty c_p(T_r-T_w)$.

Appendix C. Accuracy of the conditional skin-friction and heat-transfer decompositions

For justifying the accuracy of conditional skin-friction and heat-transfer decompositions, the variables of 200 flow fields $(\rho, \boldsymbol{u}, p)$ and their temporal derivatives are both sampled over the period $t_s u_\infty/\delta_i = 580.7$. Taking EP events, for example, the budgets of the conditionally averaged momentum equation (4.1) and energy equation (4.8) are well balanced as shown in figure 16(*a*,*b*). The error remains almost zero along the wall-normal direction, except at the wall where a small deviation is obtained. Then the balance of the conditional decompositions are checked as shown in figure 16(*c*,*d*). As the integral results

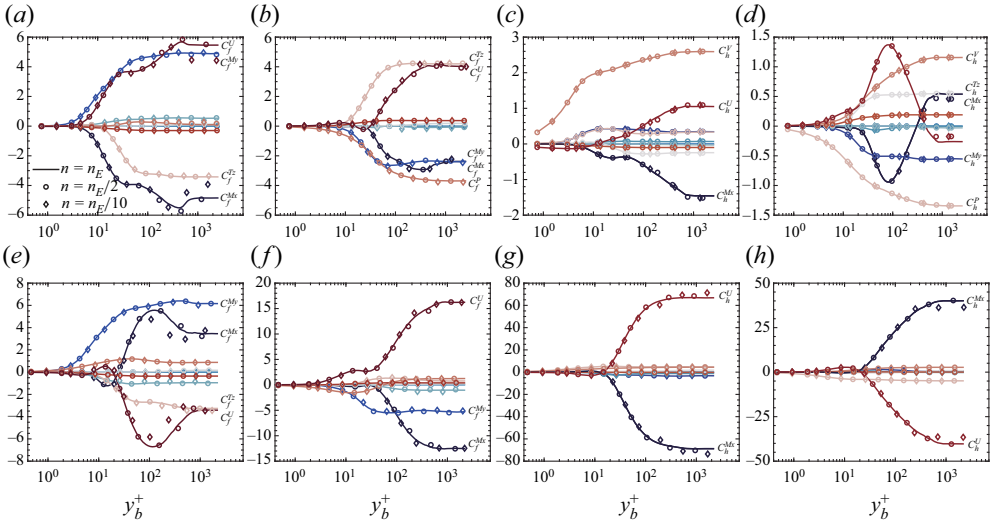

Figure 17. Dependence of the decompositions on sample numbers of extreme events n for (*a–d*) M2T05 and (*e–h*) M8T05: (*a*,*b*,*e*,*f*) components of conditionally averaged skin-friction coefficient $C_f^i(y_b)$; (*c*,*d*,*g*,*h*) components of conditionally averaged heat-transfer coefficient $C_h^i(y_b)$. Panels (*a*,*c*,*e*,*g*) and (*b*,*d*,*f*,*h*) are for EP events and EN events, respectively. The solid lines, circles and diamonds indicate sample numbers $n = n_E$, $n_E/2$ and $n_E/10$, respectively.

of the balanced conditionally averaged equations, the normalized summations of both skin-friction and heat-transfer components are consequently close to 1.0. The maximum deviation is approximately 1.6 %, which is quite acceptable. Therefore, the accuracy of conditional skin-friction and heat-transfer decompositions is proved based on the current statistics.

Appendix D. Convergence of the conditional skin-friction and heat-transfer decompositions

The statistical convergence of the conditional decompositions is checked by comparing the results based on sample numbers $n = n_E$, $n_E/2$ and $n_E/10$ with n_E referring to table 5. The dependence of the decompositions on sample numbers of extreme events n is shown in figure 17. There is good agreement between the results of $n = n_E$ (lines) and $n = n_E/2$ (circles). Meanwhile, for $n = n_E/10$ (diamonds), convergence situations vary from event to event. There remains an obvious difference between the results of $n = n_E$ and $n = n_E/10$ in certain extreme events, such as in figure 17(*a*,*e*,*g*,*h*). In short, it is guaranteed that the presently used sample number $n = n_E$ is enough for statistical convergence.

References

ADAMS, N.A. 1998 Direct numerical simulation of turbulent compression ramp flow. *Theor. Comput. Fluid Dyn.* **12** (2), 109–129.

BANNIER, A., GARNIER, É. & SAGAUT, P. 2015 Riblet flow model based on an extended fik identity. *Flow Turbul. Combust.* **95** (2), 351–376.

BERNARDINI, M., MODESTI, D., SALVADORE, F. & PIROZZOLI, S. 2021 STREAmS: a high-fidelity accelerated solver for direct numerical simulation of compressible turbulent flows. *Comput. Phys. Commun.* **263**, 107906.

BLONIGAN, P.J., FARAZMAND, M. & SAPSIS, T.P. 2019 Are extreme dissipation events predictable in turbulent fluid flows? *Phys. Rev. Fluids* **4** (4), 044606.
CARDESA, J.I., MONTY, J.P., SORIA, J. & CHONG, M.S. 2019 The structure and dynamics of backflow in turbulent channels. *J. Fluid Mech.* **880**, R3.
CHI, S.W. & SPALDING, D.B. 1966 Influence of temperature ratio on heat transfer to a flat plate through a turbulent boundary layer in air. In *International Heat Transfer Conference Digital Library*. Begel House, 41–49.
COLEMAN, G.N., KIM, J. & MOSER, R.D. 1995 A numerical study of turbulent supersonic isothermal-wall channel flow. *J. Fluid Mech.* **305**, 159–183.
DECK, S., RENARD, N., LARAUFIE, R. & WEISS, P. 2014 Large-scale contribution to mean wall shear stress in high-Reynolds-number flat-plate boundary layers up to 13 650. *J. Fluid Mech.* **743**, 202–248.
DRELA, M. 2009 Power balance in aerodynamic flows. *AIAA J.* **47** (7), 1761–1771.
DUAN, L., BEEKMAN, I. & MARTÍN, M.P. 2010 Direct numerical simulation of hypersonic turbulent boundary layers. Part 2. Effect of wall temperature. *J. Fluid Mech.* **655**, 419–445.
FARAZMAND, M. & SAPSIS, T.P. 2017 A variational approach to probing extreme events in turbulent dynamical systems. *Sci. Adv.* **3** (9), e1701533.
FUKAGATA, K., IWAMOTO, K. & KASAGI, N. 2002 Contribution of Reynolds stress distribution to the skin friction in wall-bounded flows. *Phys. Fluids* **14** (11), L73–L76.
GOMEZ, T., FLUTET, V. & SAGAUT, P. 2009 Contribution of Reynolds stress distribution to the skin friction in compressible turbulent channel flows. *Phys. Rev.* E **79** (3), 035301.
GOMIT, G., DE KAT, R. & GANAPATHISUBRAMANI, B. 2018 Structure of high and low shear-stress events in a turbulent boundary layer. *Phys. Rev. Fluids* **3** (1), 014609.
GUERRERO, B., LAMBERT, M.F. & CHIN, R.C. 2020 Extreme wall shear stress events in turbulent pipe flows: spatial characteristics of coherent motions. *J. Fluid Mech.* **904**, A18.
HIRASAKI, G.J. & HELLUMS, J.D. 1970 Boundary conditions on the vector and scalar potentials in viscous three-dimensional hydrodynamics. *Q. Appl. Maths* **28** (2), 293–296.
HOPKINS, E.J. & INOUYE, M. 1971 An evaluation of theories for predicting turbulent skin friction and heat transfer on flat plates at supersonic and hypersonic Mach numbers. *AIAA J.* **9** (6), 993–1003.
HU, S. & ZHONG, X. 1998 Linear stability of viscous supersonic plane Couette flow. *Phys. Fluids* **10** (3), 709–729.
HUANG, J., DUAN, L. & CHOUDHARI, M.M. 2022 Direct numerical simulation of hypersonic turbulent boundary layers: effect of spatial evolution and Reynolds number. *J. Fluid Mech.* **937**, A3.
HUANG, P.G., COLEMAN, G.N. & BRADSHAW, P. 1995 Compressible turbulent channel flows: DNS results and modelling. *J. Fluid Mech.* **305**, 185–218.
HUTCHINS, N. & MARUSIC, I. 2007 Large-scale influences in near-wall turbulence. *Proc. R. Soc. Lond.* A **365** (1852), 647–664.
HUTCHINS, N., MONTY, J.P., GANAPATHISUBRAMANI, B., NG, H.C. & MARUSIC, I. 2011 Three-dimensional conditional structure of a high-Reynolds-number turbulent boundary layer. *J. Fluid Mech.* **673**, 255–285.
IWAMOTO, K., FUKAGATA, K., KASAGI, N. & SUZUKI, Y. 2005 Friction drag reduction achievable by near-wall turbulence manipulation at high Reynolds numbers. *Phys. Fluids* **17** (1), 011702–011702.
JIANG, G.-S. & SHU, C.-W. 1996 Efficient implementation of weighted ENO schemes. *J. Comput. Phys.* **126** (1), 202–228.
JIMÉNEZ, J., HOYAS, S., SIMENS, M. & MIZUNO, Y. 2010 Turbulent boundary layers and channels at moderate Reynolds numbers. *J. Fluid Mech.* **657**, 335–360.
KAMETANI, Y. & FUKAGATA, K. 2011 Direct numerical simulation of spatially developing turbulent boundary layers with uniform blowing or suction. *J. Fluid Mech.* **681**, 154–172.
KAMETANI, Y., FUKAGATA, K., ÖRLÜ, R. & SCHLATTER, P. 2015 Effect of uniform blowing/suction in a turbulent boundary layer at moderate Reynolds number. *Intl J. Heat Fluid Flow* **55**, 132–142.
LENAERS, P., LI, Q., BRETHOUWER, G., SCHLATTER, P. & ÖRLÜ, R. 2012 Rare backflow and extreme wall-normal velocity fluctuations in near-wall turbulence. *Phys. Fluids* **24** (3), 035110.
LI, W., FAN, Y., MODESTI, D. & CHENG, C. 2019 Decomposition of the mean skin-friction drag in compressible turbulent channel flows. *J. Fluid Mech.* **875**, 101–123.
MARLEY, C.D. & RIGGINS, D.W. 2011 Numerical study of novel drag reduction techniques for hypersonic blunt bodies. *AIAA J.* **49** (9), 1871–1882.
MEHDI, F., JOHANSSON, T.G., WHITE, C.M. & NAUGHTON, J.W. 2014 On determining wall shear stress in spatially developing two-dimensional wall-bounded flows. *Exp. Fluids* **55** (1), 1–9.
MODESTI, D., PIROZZOLI, S., ORLANDI, P. & GRASSO, F. 2018 On the role of secondary motions in turbulent square duct flow. *J. Fluid Mech.* **847**, R1.

MORKOVIN, M.V. 1962 Effects of compressibility on turbulent flows. *Méc. Turbul.* **367** (380), 26.
NAGIB, H.M., CHAUHAN, K.A. & MONKEWITZ, P.A. 2007 Approach to an asymptotic state for zero pressure gradient turbulent boundary layers. *Proc. R. Soc. Lond.* A **365** (1852), 755–770.
PAN, C. & KWON, Y. 2018 Extremely high wall-shear stress events in a turbulent boundary layer. *J. Phys.: Conf. Ser.* **1001**, 012004.
PEET, Y. & SAGAUT, P. 2009 Theoretical prediction of turbulent skin friction on geometrically complex surfaces. *Phys. Fluids* **21** (10), 105105.
PIROZZOLI, S. 2010 Generalized conservative approximations of split convective derivative operators. *J. Comput. Phys.* **229** (19), 7180–7190.
PIROZZOLI, S. & BERNARDINI, M. 2011 Turbulence in supersonic boundary layers at moderate Reynolds number. *J. Fluid Mech.* **688**, 120–168.
PIROZZOLI, S. & BERNARDINI, M. 2013 Probing high-Reynolds-number effects in numerical boundary layers. *Phys. Fluids* **25** (2), 021704.
PIROZZOLI, S., BERNARDINI, M. & GRASSO, F. 2010 Direct numerical simulation of transonic shock/boundary layer interaction under conditions of incipient separation. *J. Fluid Mech.* **657**, 361–393.
POINSOT, T.J. & LELE, S.K. 1992 Boundary conditions for direct simulations of compressible viscous flows. *J. Comput. Phys.* **101** (1), 104–129.
RENARD, N. & DECK, S. 2016 A theoretical decomposition of mean skin friction generation into physical phenomena across the boundary layer. *J. Fluid Mech.* **790**, 339–367.
ROY, C.J. & BLOTTNER, F.G. 2006 Review and assessment of turbulence models for hypersonic flows. *Prog. Aerosp. Sci.* **42** (7–8), 469–530.
RUMSEY, C.L. 2010 Compressibility considerations for k-ω turbulence models in hypersonic boundary-layer applications. *J. Spacecr. Rockets* **47** (1), 11–20.
SHENG, J., MALKIEF, E. & KATZ, J. 2009 Buffer layer structures associated with extreme wall stress events in a smooth wall turbulent boundary layer. *J. Fluid Mech.* **633**, 17–60.
SPALART, P.R., MOSER, R.D. & ROGERS, M.M. 1991 Spectral methods for the Navier–Stokes equations with one infinite and two periodic directions. *J. Comput. Phys.* **96** (2), 297–324.
SPINA, E.F., SMITS, A.J. & ROBINSON, S.K. 1994 The physics of supersonic turbulent boundary layers. *Annu. Rev. Fluid Mech.* **26** (1), 287–319.
STROH, A., HASEGAWA, Y., SCHLATTER, P. & FROHNAPFEL, B. 2016 Global effect of local skin friction drag reduction in spatially developing turbulent boundary layer. *J. Fluid Mech.* **805**, 303–321.
SUBBAREDDY, P. & CANDLER, G. 2011 DNS of transition to turbulence in a hypersonic boundary layer. In *41st AIAA Fluid Dynamics Conference and Exhibit*, AIAA paper, p. 3564.
TANG, J., ZHAO, Z., WAN, Z.-H. & LIU, N.-S. 2020 On the near-wall structures and statistics of fluctuating pressure in compressible turbulent channel flows. *Phys. Fluids* **32** (11), 115121.
TONG, F., DONG, S., LAI, J., YUAN, X. & LI, X. 2022 Wall shear stress and wall heat flux in a supersonic turbulent boundary layer. *Phys. Fluids* **34** (1), 015127.
VAN DRIEST, E.R. 1956 On turbulent flow near a wall. *J. Aeronaut. Sci.* **23** (11), 1007–1011.
WALLACE, J.M. 2016 Quadrant analysis in turbulence research: history and evolution. *Annu. Rev. Fluid Mech.* **48**, 131–158.
WALZ, A. 1969 *Boundary Layers of Flow and Temperature*. MIT Press.
WENZEL, C., GIBIS, T. & KLOKER, M. 2022 About the influences of compressibility, heat transfer and pressure gradients in compressible turbulent boundary layers. *J. Fluid Mech.* **930**, A1.
XU, D., WANG, J. & CHEN, S. 2022 Skin-friction and heat-transfer decompositions in hypersonic transitional and turbulent boundary layers. *J. Fluid Mech.* **941**, A4.
XU, D., WANG, J., WAN, M., YU, C., LI, X. & CHEN, S. 2021 Effect of wall temperature on the kinetic energy transfer in a hypersonic turbulent boundary layer. *J. Fluid Mech.* **929**, A33.
YU, M., LIU, P., FU, Y., TANG, Z. & YUAN, X. 2022 Wall shear stress, pressure, and heat flux fluctuations in compressible wall-bounded turbulence. Part 1. One-point statistics. *Phys. Fluids* **34** (6), 065139.
YU, M., XU, C.-X. & PIROZZOLI, S. 2019 Genuine compressibility effects in wall-bounded turbulence. *Phys. Rev. Fluids* **4** (12), 123402.
YU, M., XU, C.-X. & PIROZZOLI, S. 2020 Compressibility effects on pressure fluctuation in compressible turbulent channel flows. *Phys. Rev. Fluids* **5** (11), 113401.
ZHANG, C., DUAN, L. & CHOUDHARI, M.M. 2017 Effect of wall cooling on boundary-layer-induced pressure fluctuations at Mach 6. *J. Fluid Mech.* **822**, 5–30.
ZHANG, C., DUAN, L. & CHOUDHARI, M.M. 2018 Direct numerical simulation database for supersonic and hypersonic turbulent boundary layers. *AIAA J.* **56** (11), 4297–4311.
ZHANG, P., SONG, Y. & XIA, Z. 2022*a* Exact mathematical formulas for wall-heat flux in compressible turbulent channel flows. *Acta Mechanica Sin.* **38** (1), 1–10.

ZHANG, P. & XIA, Z. 2020 Contribution of viscous stress work to wall heat flux in compressible turbulent channel flows. *Phys. Rev.* E **102** (4), 043107.

ZHANG, P.-J.-Y., WAN, Z.-H., LIU, N.-S., SUN, D.-J. & LU, X.-Y. 2022*b* Wall-cooling effects on pressure fluctuations in compressible turbulent boundary layers from subsonic to hypersonic regimes. *J. Fluid Mech.* **946**, A14.

ZHANG, P.-J.-Y., WAN, Z.-H. & SUN, D.-J. 2019 Space-time correlations of velocity in a Mach 0.9 turbulent round jet. *Phys. Fluids* **31** (11), 115108.

ZHANG, S., LI, X., ZUO, J., QIN, J., CHENG, K., FENG, Y. & BAO, W. 2020 Research progress on active thermal protection for hypersonic vehicles. *Prog. Aerosp. Sci.* **119**, 100646.

ZHANG, Y.-S., BI, W.-T., HUSSAIN, F. & SHE, Z.-S. 2014 A generalized Reynolds analogy for compressible wall-bounded turbulent flows. *J. Fluid Mech.* **739**, 392–420.

ZHAO, X. & HE, G.-W. 2009 Space-time correlations of fluctuating velocities in turbulent shear flows. *Phys. Rev.* E **79** (4), 046316.